ULTRASONIC VISCOELASTICITY IMAGING OF pH IN BIOPOLYMERS

BY

REBECCA DAWN YAPP

B.S., Illinois State University, 2004

THESIS

Submitted in partial fulfillment of the requirements
for the degree of Master of Science in Bioengineering
in the Graduate College of the
University of Illinois at Urbana-Champaign, 2008

Urbana, Illinois

Adviser:

Professor Michael F. Insana

Abstract

Understanding contrast mechanisms and identifying discriminating features is at the heart of diagnostic imaging development. This thesis focuses on how pH influences the viscoelastic properties of biopolymers to better understand the effects of extracellular pH on breast tumor elasticity imaging. Extracellular pH is known to decrease as much as 1 pH unit in breast tumors, thus creating a dangerous environment that increases cellular mutate rates and therapeutic resistance. We used a gelatin hydrogel phantom to isolate the effects of pH on a polymer network with similarities to the extracellular matrix in breast stroma. Using compressive unconfined creep and stress relaxation measurements, we systematically measured the viscoelastic features sensitive to pH by way of time domain models and complex modulus analysis. Methods for obtaining estimates of the complex modulus from the time domain measurements are described in detail. The results of creep and stress relaxation measurements are used to determine the sensitivity of quasi-static ultrasonic elasticity imaging to pH. We found a strong elastic response of the polymer network to pH, such that the matrix stiffness decreases as pH was reduced, however the viscous response of the medium to pH was negligible. These observations suggest that the large contrast common in breast tumors with desmoplasia can be reduced under acidic conditions, and that viscoelastic features are unlikely to improve discriminability.

To my fiancé Dan, Mom, Dad, and sister Rachel.

Acknowledgments

Thank you Dr. Michael Insana for your guidance, providing me with the opportunity to work with you, and being a great mentor. Thank you Dr. Mallika Sridhar for all your help and guidance with many aspects of this work. Thanks to Peggy Qiu and David Mahr for assistance with elasticity imaging algorithms and instrumentation. Thanks to Dan Sherman for always being supportive, and for your help machining parts. Finally, thanks to my family and friends for all the support and encouragement.

This work is based upon work supported by the National Cancer Institute under award number ROI CA082497. Portions of this thesis are reprinted with permission from: R. D. Yapp and M. F. Insana. pH induced contrast in viscoelasticity imaging of biopolymers. *Physics in Medicine and Biology*, in review, ©[2008 IOP].

Table of Contents

Chapter 1

Introduction

Elasticity imaging continues to mature as a tool for breast cancer diagnosis because of its unique ability to describe mechanical properties of soft tissues. The excitement about diagnostic elasticity imaging stems from the large increase in stiffness (or equivalently a reduction in elastic strain) commonly associated with tumors. Specifically, elasticity imaging is able to image the characteristic signature of desmoplasia that is often specific to malignancies [13]. Nevertheless many early-stage lesions, some as large as 2 cm, do not change stiffness, which suggests a need to increase the mechanical feature space for diagnosis [26, 28]. To realize the diagnostic potential of elasticity imaging, researchers must improve knowledge of the mechanisms by which breast diseases generate elasticity contrast.

Several groups are studying contrast mechanisms through different approaches to elasticity imaging. Each shares the aim of exploring viscoelastic (VE) properties of soft biological tissues for diagnosis. In quasi-static elasticity imaging methods used in our lab [33], a force on the order of 4 N is suddenly applied to tissues in about 1 s and held constant for 10 to 200 s while frames of radio frequency (RF) echo signals are recorded. The RF signals are analyzed to track tissue movements and thus generate a time-series of strain images. To estimate VE parameters, we fit rheological model functions obtained via constitutive equations to the time-varying strain data. The slow timing of the applied ramp-and-hold force means that stress stimuli are applied at very low frequencies (quasi-static), typically in a bandwidth below 1 Hz. Dynamic methods [31, 32], in contrast, apply much lower forces at much higher force-stimulation frequencies (>50Hz), which is significant because hydrogels, including breast stroma and other connective tissues, exhibit frequency dependent material properties [10]. In this report, we study the effects of pH on gelatin hydrogel dynamics at force frequencies between 10^{-3} and 10^{-1} rad/s. Our goal is to explore the sensitivity of quasi-static elasticity methods for imaging pH-sensitive VE properties in tissue-like media.

What occurs in breast tumors that could change VE properties? The answer originates with the molecular biology of cancer. Malignant mammary epithelial cells initiate a cascade of signaling

pathways that interact with the extracellular matrix (ECM) of breast stroma to stimulate tumor cell proliferation, differentiation, adhesion, and concomitant support systems such as neoangiogenesis [9]. Breast stroma, the supporting matrix of mammary tissue that determines mechanical properties, is known to play an active role in processes leading to malignant progression [8]. Depending on microenvironmental factors in the stroma, cell growth can be rapid and chaotic, thus producing heterogeneous, hypoxic neoplasms with acidic regions where growth has outpaced the nutrient supply and waste removal provided by regional blood flow. Irregular perfusion and increased lactic acid secretion by tumor cells produces pH gradients across cell membranes as large as 0.6 pH units [14], and extracellular pH (pH_e) gradients up to 1 pH unit across a 1 cm distance [15]. Acidic conditions are dangerous microenvironmental factors because they increase the rate of malignant cell transformation, in vivo metastasis, and the resistance to conventional therapeutics.

Variations in pH from the isoelectric pH (IEP) value[1] are also known to alter the matrix structure of many hydropolymers [39], including connective tissues, and thus the VE properties [29, 30, 38]. Isolated ECM proteins have a net negative surface charge. They self assemble in situ with conformations that seek stability near the IEP. We are investigating the role of pH on the VE properties of hydrogels so as to begin to understand its role in generating breast tumor elasticity contrast. The ECM of stroma undergoes a constant reorganization and growth during cancer progression. Therefore temporal variations in tumor pH_e are expected to generate a spatiotemporal modulation of structural ECM change. For hydrogels to be useful at modeling this situation, we need to modify the pH away from its IEP during polymerization.

Gelatin hydrogels were previously investigated as simple physical models of breast stroma in order to validate our elastic imaging techniques [34]. Although there are major differences between the structures of gelatin and ECM polymers, comparisons of their VE properties show that gelatin hydrogels can be a reasonable model for breast tissues [33, 35]. The fibril form of natural type I collagen in stromal ECM is a highly ordered elastic structure, stabilized by hydrogen and electrostatic bonds within and among the proteins. In addition to the net negative surface charge, hydrophilic proteoglycan molecules aid in structuring fluid in the collagenous matrix [36]. In the denatured form of collagen, gelatin forms a less ordered elastic aggregate network containing polar side chains that aid in structuring fluids to form a hydrogel.

This thesis focuses on obtaining imaging parameters sensitive to the pH induced contrast in gelatin hydrogels. These parameters are estimated by applying time domain models to classical

[1]The IEP is the pH at which a polypeptide has zero net charge [2].

mechanical techniques, unconfined uniaxial creep and stress relaxation. The mechanical tests are performed on homogeneous gel samples constructed at pH levels about the IEP. The acquired time domain data can also be used to estimate the frequency dependent material properties, specifically the complex modulus $E^*(\omega)$. This frequency domain information can be used as a tool for interpretation of pH induced contrast. Quasi-static elasticity methods used in our lab take the form of an unconfined uniaxial creep experiment, thus pH sensitive parameters estimated from creep measurements on gel samples can be directly related to the elasticity imaging study. To model pH induced changes in diseased breast stroma, a gel phantom of heterogeneous pH distribution is constructed to assess the sensitivity of elasticity imaging to pH induced changes. In this thesis, results as well as processing methods are discussed for both time and frequency domain analysis. The goal of this study is to determine the degree to which quasi-static elasticity imaging is sensitive to pH changes in hydrogels and to understand sources of pH-induced contrast. Gel data are used to begin evaluating the role of pH changes in diseased breast stroma.

Chapter 2

Theory

In this chapter, the constitutive equations governing the mechanical testing and elasticity imaging experiments are described. Followed by a discussion of the data processing techniques used in this study for both the time and frequency domain.

2.1 Constitutive Equations

The two types of transient mechanical experiments performed on gelatin hydrogels were creep and stress relaxation. The primary focus was on creep because we can image the strain response. The stress relaxation experiment, which mechanically stimulates the gel with a strain rather than a stress, was used because it provides an alternative perspective of the material properties. Creep tests performed on homogenous gel samples share the same experimental geometry as elasticity imaging studies. To avoid confusion, the results of creep experiments performed on homogenous gel samples will be referred to as 'creep' measurements and those of elasticity imaging experiments will be referred to as 'elasticity imaging' measurements from this point forward.

In this study, creep tests took the form of unconfined uniaxial compression, where the stress σ_a was applied to the top surface of the specimen in about 1 s and held for at least 1800 s. Since the gels behave as viscoelastic polymers, they constantly dissipate the applied stress with time. To compensate for this loss and maintain a constant applied stress, the specimen was increasingly strained. To get a measure of the viscoelastic properties of the material during a creep test we monitored the strain $\varepsilon(t)$ as a function of time, as illustrated in figure 2.1a. These creep tests were performed on both the homogenous gel samples and the elasticity imaging phantoms.

The stress relaxation test was only performed on the homogeneous gel samples. It is also an unconfined uniaxial compression test, where the applied strain ε_a was applied to the top surface of the specimen in about 1 s and held for 3600 s. Upon application of strain, the gel is stressed, but again, by the viscoelastic nature of the gels this stress is dissipated with time. We measured the

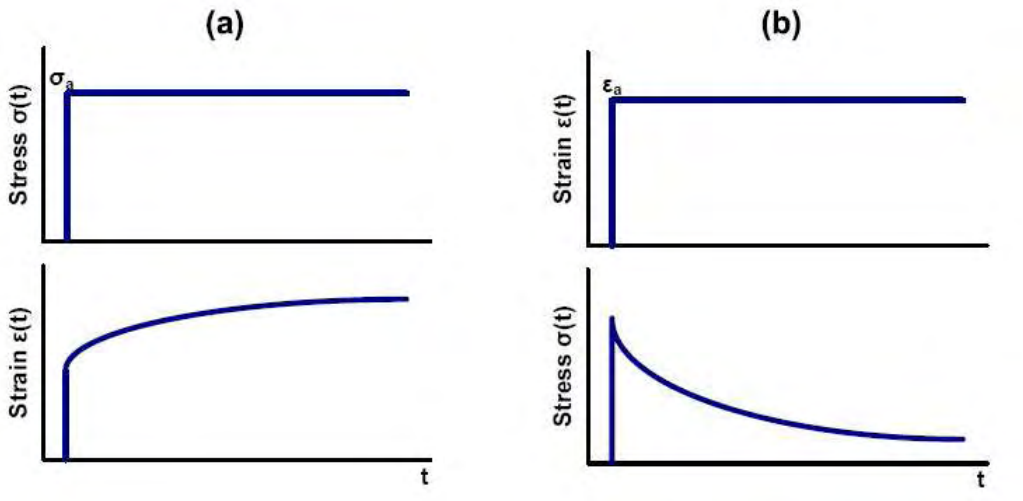

Figure 2.1: **(a)** is a schematic of creep experiment and **(b)** is a schematic of a stress relaxation experiment.

stress $\sigma(t)$ to monitor the viscoelastic properties of the gel in a stress relaxation test as illustrated in figure 2.1b. Detailed descriptions of the relevant constitutive equations for these experiments are described elsewhere [34]. The constitutive equations were applied in the development of rheological models to parameterize creep data for imaging. The following descriptions are specific to results in this thesis.

The constitutive equation for uniaxial compressive creep is given by,

$$\varepsilon(t) = \int_0^t \frac{\partial \sigma(t')}{\partial t'} D(t - t')dt', \tag{2.1}$$

where $\varepsilon(t)$ is the strain response along the axis of $\sigma(t)$, the uniaxial applied stress, and $D(t)$ is the compressive compliance. The frequency response $\tilde{\varepsilon}(\omega)$ of equation 2.1 is found from the Fourier transform,

$$\tilde{\varepsilon}(\omega) = i\omega\tilde{\sigma}(\omega)\tilde{D}(\omega), \tag{2.2}$$

where $\tilde{\varepsilon}(\omega)$, $\tilde{\sigma}(\omega)$, and $\tilde{D}(\omega)$ are the Fourier transforms of $\varepsilon(t)$, $\sigma(t)$, and $D(t)$ respectively, and $i = \sqrt{-1}$. The frequency dependent material properties are described by the complex modulus $E^*(\omega)$ or the complex compliance $D^*(\omega)$, which are related to the transient experiments by equation 2.3,

$$i\omega\tilde{D}(\omega) = \frac{\tilde{\varepsilon}(\omega)}{\tilde{\sigma}(\omega)} = \frac{1}{E^*(\omega)} = \frac{1}{E'(\omega) + iE''(\omega)} = D^*(\omega) = D'(\omega) - iD''(\omega) \tag{2.3}$$

where $E'(\omega)$ and $E''(\omega)$ are the real and imaginary parts of $E^*(\omega)$ respectively; and $D'(\omega)$ and $D''(\omega)$ are the real and imaginary parts of $D^*(\omega)$ respectively [12,37,42]. It is advantageous to analyze the frequency domain data $E^*(\omega)$ because it provides separable information about mechanical energy stored (real part) and lost (imaginary part) [10]; which emphasizes the elastic and viscous components.

A similar analysis is applied to the stress relaxation test. The constitutive equation governing the stress relaxation test is given in equation 2.4,

$$\sigma(t) = \int_0^t \frac{\partial \varepsilon(t')}{\partial t'} E(t-t')dt' \tag{2.4}$$

where $E(t)$ is the compressive modulus. The complex modulus, $E^*(\omega)$ can also be estimated [37,42] from the stress data by the following:

$$i\omega\tilde{E}(\omega) = \frac{\tilde{\sigma}(\omega)}{\tilde{\varepsilon}(\omega)} = E^*(\omega) \tag{2.5}$$

where $\tilde{E}(\omega)$ is the Fourier transform of $E(t)$.

2.2 Data Processing Techniques

Viscoelastic parameters estimated from the strain data of quasi-static elasticity imaging studies typically assume the stress was applied in the form $\sigma(t) = \sigma_a u(t)$ [35,40] where $u(t)$ is the unit step function. Experimentally, it is not possible to achieve a unit step input for creep or stress relaxation measurements; instead the input for creep is in the form $\sigma(t) = \sigma_a r_{t_0}(t)$ where $r_{t_0}(t)$ is the unit ramp function (see equation 2.6), with ramp time t_0. Similarly for stress relaxation the input strain takes the form $\varepsilon(t) = \varepsilon_a r_{t_0}(t)$.

$$r_{t_0}(t) = \begin{cases} 0 & , t \leq 0 \\ t/t_0 & , 0 \leq t \leq t_0 \\ 1 & , t \geq t_0 \end{cases} \tag{2.6}$$

The time of the ramp (t_0) in the studies presented here is typically about 1 s, which is very small compared to the total experiment times of 1800 s or greater. In this study, the assumption of a step input is used to study creep and stress relaxation measurements in order to estimate pH sensitive parameters for elasticity imaging. The short time ramp used in these studies has little effect on

the time domain processing; however, the effect of the ramp input on $E^*(\omega)$ and $D^*(\omega)$ is more severe as discussed in section 2.2.1. $E^*(\omega)$ and $D^*(\omega)$ are estimated from creep and stress relaxation measurements via two different approaches.

Approach 1 Assume that the ramp input is a step input.

Approach 2 Analyze all the data, including the ramp.

The following sections describe these processing approaches as they apply to time and frequency domain processing of creep and stress relaxation measurements.

2.2.1 Approach 1

Processing using this approach assumes the ramp input of creep or stress relaxation measurements is approximately a step input. Both time and frequency domain processing are considered. Time domain processing using approach 1 was used for creep and stress relaxation measurements for estimating pH sensitive contrast parameters for elasticity imaging. The time domain discussion of creep measurements processed using approach 1 also applies to the elasticity imaging measurements.

Approach 1: Creep

When processing time domain creep data under approach 1, the stress is assumed to be applied as a step function $\sigma(t) \cong \sigma_a u(t)$. For example, if the stress was applied in 1 s, then the stress and strain data would be analyzed starting 1 s into the acquisition. The time vector would be corrected to make the assumption that this 1 s starting point occurs at 0 s. To illustrate, see figure 2.2a in which the circled part of the data is kept and assumed to start at time $t = 0$ s and the ramp data (not circled) is discarded. Substituting $\sigma(t) = \sigma_a u(t)$ into equation 2.1 gives

$$\begin{aligned} \varepsilon(t) &= \int_0^t \frac{\partial(\sigma_a u(t'))}{\partial t'} D(t-t')dt' && (2.7) \\ &= \int_0^t \sigma_a \delta(t') D(t-t')dt' && (2.8) \\ &= \sigma_a D(t) && (2.9) \end{aligned}$$

where $\delta(t)$ is the Dirac delta function. Thus, this approximation results in a simple linear relationship between compressive compliance and experimental strain data.

Based upon previous experience with creep tests on gelatin gels, the time domain strain response is well modeled by a generalized Voigt model. This complex polymer network likely has a contribu-

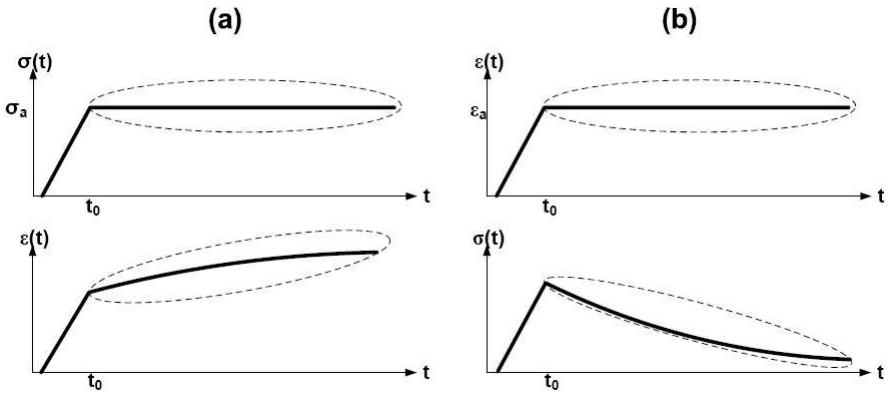

Figure 2.2: This figure displays what part of the experimental data (circled region) is analyzed under approach 1 for a creep experiment **(a)** and a stress relaxation experiment **(b)**.

tion from a continuum of responses as described by equation 2.10. A discrete version of the model as shown in equation 2.11 is a good approximation that can be used to parameterize the material response by focusing on only the K largest eigenvalues [35]. ε_0 is the strain amplitude of the initial elastic response, and the parameters ε_k and T_k represent the amplitudes and time constants of the VE components, respectively, for each discrete Voigt element. Previously [34, 41] it was shown that a bi-exponential model with a linear component representing a purely viscous response ($\beta = \sigma_a/\eta_0$, where η_0 is the viscosity coefficient) was a good approximation to experimental data as seen in equation 2.12. However, new evidence suggests this linear component is a viscoelastic element with $T_3 \gg T_1, T_2$. Thus, in this study we modeled the creep response with a tri-exponential Voigt model with $\beta = \varepsilon_3/T_3$ representing the $k = 3$ viscoelastic component approximated from its first order Taylor Series expansion. A graphical representation of the discrete components of equation 2.12 is presented in figure 2.3.

$$\varepsilon(t) = \varepsilon_0 + \int_0^t d\tau \acute{\varepsilon}(\tau)\left(1 - \exp\left(-\frac{\tau}{T}\right)\right) \tag{2.10}$$

$$\simeq \varepsilon_0 + \sum_{k=1}^{K} \varepsilon_k \left(1 - \exp\left(-\frac{t}{T_k}\right)\right) \tag{2.11}$$

$$\simeq \varepsilon_0 + \sum_{k=1}^{2} \varepsilon_k \left(1 - \exp\left(-\frac{t}{T_k}\right)\right) + \beta t \tag{2.12}$$

The motivation for modeling creep data in this matter was we are interested in the VE response to a step stress and the curve fitting routine is optimal when the number of parameters is minimized. The tri-exponential model (equation 2.12) was fit to experimental data by first estimating and subtracting

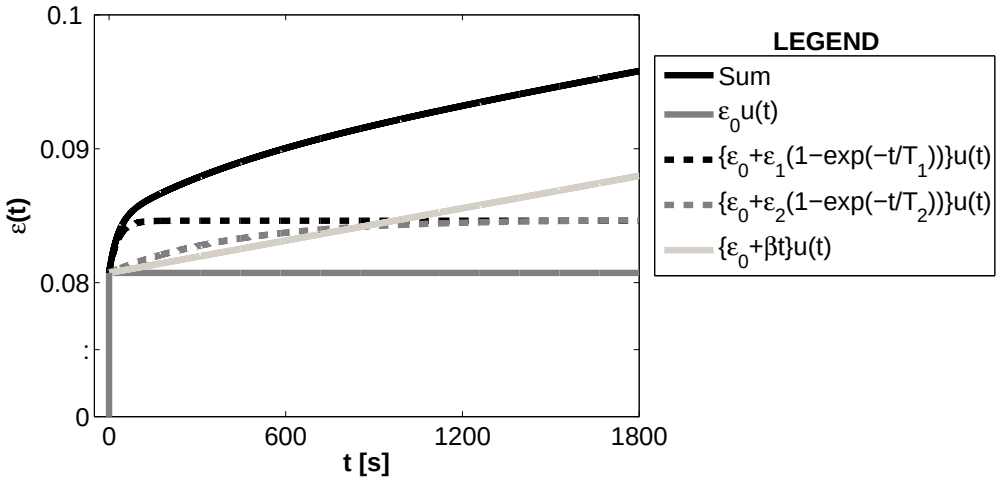

Figure 2.3: This figure displays a graphical representation of the discrete components of equation 2.12; where 'Sum' refers to equation 2.12, which is the superposition of the components. The other components presented are as indicated in the legend.

the linear component βt from the creep data, followed by fitting the residual time domain strain data to a discrete bi-exponential Voigt model as described elsewhere [34, 35] using the Matlab function `LSQCURVEFIT`. The linear term was estimated by taking a second derivative of $\varepsilon(t)$ to find a time range where the data is zero. The corresponding range in the $\varepsilon(t)$ data was then fit to a 1st order polynomial with its slope representing β. Then the linear term βt was removed from $\varepsilon(t)$ and the slope of the residual strain data at long times was checked to ensure that it was non-negative. If the slope at long times was negative, β was corrected until a zero slope was achieved.

Under approach 1, this discrete element Voigt model (equation 2.12) can also be written in terms of compressive compliance $D(t)$ and represented as a superposition of elastic, viscoelastic, and linear responses as:

$$D(t) = D_E(t)+D_{VE}(t)+D_L(t) \text{ , where } \begin{cases} D_0 u(t) & \text{, } D_E(t) \text{ (Elastic)} \\ \sum_{k=1}^{K} D_k \left(1 - \exp\left(-\frac{t}{T_k}\right)\right) u(t) & \text{, } D_{VE}(t) \text{ (Viscoelastic)} \\ \frac{\beta}{\sigma_a} t u(t) & \text{, } D_L(t) \text{ (Linear)} \end{cases} \tag{2.13}$$

where $\varepsilon_k = \sigma_a D_k$ for $k = 0, 1, 2, ..., K$ according to the relationship between compressive compliance and strain given by equation 2.9. By representing creep data in this manner, it is possible to delineate any of the responses from the total. For instance, to analyze the purely elastic response we would simply take the value of $D(t)|_{t=0} = D_0 = D_E$.

Under Approach 1, it is possible to analyze the frequency response $E^*(\omega)$ by taking the Fourier transform of the derivative of $D(t)$ according to the relationships given in equations 2.3 and 2.9 to obtain $D^*(\omega)$. Because of the inverse relationship, $E^*(\omega)$ can be obtained from $D^*(\omega)$. The separable nature of this Voigt model in the time domain (see equation 2.13) makes it possible to analyze the frequency response in a number of ways. There are three interpretations of the complex modulus data we are interested in:

a. $E^*(\omega)$ for $D(t) = D_E + D_{VE} + D_L$

b. $E^*(\omega)$ for $D(t) = D_E + D_{VE}$

c. $E^*(\omega)$ for $D(t) = D_{VE}$.

Case **a** provides the frequency dependent material properties for the total mechanical response. This interpretation is useful when comparing the spectra obtained for $E^*(\omega)$ from both stress relaxation and creep measurements (see section 2.2.1 **Approach 1: Stress Relaxation**). Case **b** provides analysis of a stable system. The linear component ($D_L(t)$) results in a pole at $s = 0$ in the Laplace domain, thus its removal results in a stable system[2]. Finally, case **c** is useful for interpretation of the purely viscoelastic response. This case is particularly useful for parameterizing the material response using a fractional derivative technique as described by Coussot et al. [5].

To process cases **a**, **b**, or **c** a derivative of $D(t)$ is taken followed by the Fourier transform of this derivative data as instructed by equation 2.3 to obtain $D^*(\omega)$. $E^*(\omega)$ is then obtained by inverting $D^*(\omega)$. There are some notable processing complications that arise when processing in this manner due to complications with the derivative approximation and the limitation of being able to only process injective functions. To be clear on the steps taken to avoid incorrect frequency domain processing, each case is described individually and can be found in appendix A.1.1.

Approach 1: Stress Relaxation

When processing time domain stress relaxation data under approach 1, the strain is assumed to be applied as a step function with amplitude ε_a. Similar to the creep data, if the ramp was applied in t_0 seconds, then the data starting at $t = t_0$ would be assumed to start at $t = 0$ seconds as illustrated in figure 2.2b. By adjusting the data in this manner, the input strain is then $\varepsilon(t) = \varepsilon_a u(t)$, which results in a linear relationship between the measured output stress $\sigma(t)$ and the compressive modulus

[2]Experimental creep and stress relaxation measurements can be represented using one-sided Laplace transforms, with Laplace variable s, and are related to the frequency domain for $s = i\omega$

$E(t)$ as seen in equation 2.14, which is derived from equation 2.4 in a similar manner to the creep data.

$$\sigma(t) = \varepsilon_a E(t) \tag{2.14}$$

The stress relaxation test can be well modeled with a Maxwell model [37]. Alfrey's rules tell us how to choose the appropriate components for the Maxwell model, based upon the Voigt model chosen for creep experiments [34, 37]. Based upon these rules and equation 2.13, the corresponding Maxwell model for stress relaxation experiments is,

$$E(t) = \sum_{l=1}^{L} E_l \exp\left(-\frac{t}{\tau_l}\right) \tag{2.15}$$

where E_l and τ_l represent the amplitude and time constants respectively of the viscoelastic Maxwell units.

Unlike the Voigt model, the Maxwell model does not allow for easy separation of elastic and viscoelastic components. For example, to analyze the elastic response, the value of $E(t)|_{t=0} = E_0 = \sum E_l$. Thus, the analysis of this type of experiment can only be done for all the contributing components simultaneously like case **a** for the creep experiment under approach 1. Similar to the creep experiment, a derivative of $E(t)$ is taken followed by the Fourier transform to obtain $E^*(\omega)$. There are some processing complications associated with this method described in detail in the appendix A.1.2.

Approach 1: Effect of Ramp

In this section the error associated with the output strain or stress data in creep and stress relaxation measurements due to assuming the applied ramp input is a step input is described. The Fourier transforms of compliance and modulus from stress relaxation and creep experiments are related by $\tilde{D}(\omega)\tilde{E}(\omega) = 1/(i\omega)^2$. In the time domain, the initial elastic response (IER) provides an estimate of the elastic modulus E_0 under approach 1; eg. the elastic modulus $E_0 = E(t=0) = \sigma(t=0)/\varepsilon_a$ is found from stress relaxation data, and is related to the elastic compliance $D_0 = D(t=0) = \varepsilon_0/\sigma_a = 1/E_0$ estimated from the creep data. This inverse relationship between $E(t)$ and $D(t)$ only holds when the material response behaves as an elastic material [11, 34, 37]; then $D(t)E(t) \simeq 1$. In the case of an applied step stress or strain, the input is so fast that the viscous response does not have time to react, thus for time 0, the IER provides an estimate of E_0. The effect of the ramp on E_0 estimates are minor and are discussed in terms of the experimental results in section 4.1.1. This

discussion will focus on the frequency domain complications.

For approach 1 processing of creep data, we assume that our strain data was acquired as a result of an applied step stress even though a ramp stress is typically applied within 1 s. The following description provides insight into the problems associated with this assumption in creep data. If a step stress, $\sigma_a u(t)$ with Fourier transform $\sigma_a/i\omega$, was applied, the corresponding complex compliance would be $D^*_{step}(\omega) = i\omega\tilde{\varepsilon}_{step}(\omega)/\sigma_a$, where $D^*_{step}(\omega)$ and $\tilde{\varepsilon}_{step}(\omega)$ are the complex compliance and Fourier transform of the measured strain data respectively when a step input stress is assumed. When a ramp stress is applied, $\sigma(t) = \sigma_a r_{t_0}(t)$, the corresponding complex compliance is

$$D^*_{ramp}(\omega) = \frac{t_0(i\omega)^2\tilde{\varepsilon}_{ramp}(\omega)}{\sigma_a(1-\exp(-t_0 i\omega))} \tag{2.16}$$

where $D^*_{ramp}(\omega)$ and $\tilde{\varepsilon}_{ramp}(\omega)$ are the complex compliance and Fourier transform of the measured strain data, respectively, when a ramp input stress is assumed.

What we measure experimentally is $\varepsilon_{ramp}(t)$ but we assume that this is $\varepsilon_{step}(t)$. Therefore what we have is an approximation of the complex compliance $D^*_A(\omega)$ according to equation 2.17 where $D^*(\omega)$ is the true complex compliance of the system.

$$D^*_A(\omega) = \frac{i\omega\tilde{\varepsilon}_{ramp}(\omega)}{\sigma_a} = \frac{D^*(\omega)(1-\exp(-i\omega t_0))}{i\omega t_0} \tag{2.17}$$

Thus the error $Er(\omega)$ associated with $D^*_A(\omega)$ is the multiplication of $Er(\omega)$ by the true $D^*(\omega)$.

$$Er(\omega) = \frac{1-\exp(-i\omega t_0)}{i\omega t_0} \tag{2.18}$$

To better understand how this error will affect the $D^*(\omega)$ estimation, we can rewrite equation 2.17 in terms of its real (storage) and imaginary (loss) parts as,

$$D'_A(\omega) = D'(\omega)Er'(\omega) + D''(\omega)Er''(\omega) \tag{2.19a}$$

$$D''_A(\omega) = D''(\omega)Er'(\omega) - D'(\omega)Er''(\omega) \tag{2.19b}$$

where $Er'(\omega) = \frac{\sin(\omega t_0)}{\omega t_0}$ is the real component of $Er(\omega)$, and $Er''(\omega) = \frac{\cos(\omega t_0)-1}{\omega t_0}$ is the imaginary component of $Er(\omega)$. As $t_0 \to 0$, $\cos(\omega t_0) \to 1$, therefore $Er''(\omega)$ goes to zero; and by small angle approximation, $\sin(\omega t_0) \to \omega t_0$, therefore $D''_A(\omega) \approx D''(\omega)$ and $D'_A(\omega) \approx D'(\omega)$. A typical experiment for creep utilizes a $t_0 = 1$ s ramp for the applied stress. Under this condition, it can be

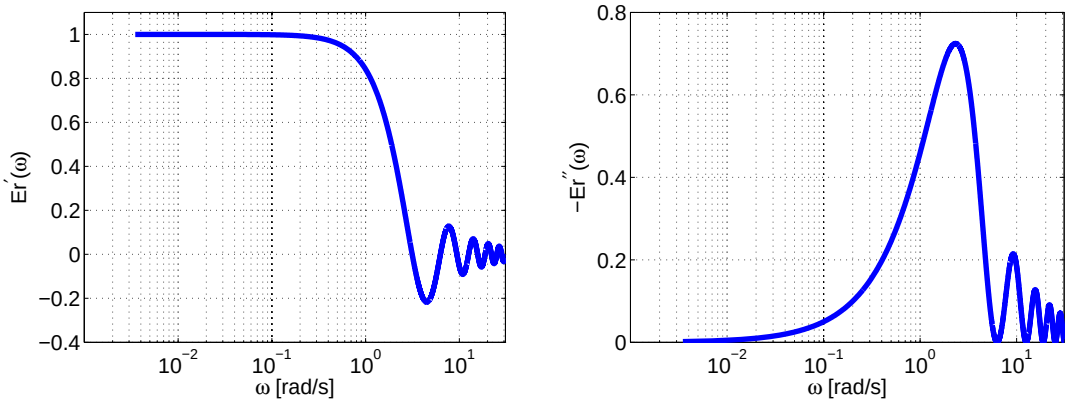

Figure 2.4: Error associated with a ramp stress or strain with $t_0 = 1$ s for a creep or stress relaxation experiment.

seen from figure 2.4 that for $\omega \approx 0.1$ rad/s, $Er'(\omega) \approx 1$ and $Er''(\omega)$ is approaching 0. Based upon this analysis, it is reasonable to analyze spectra for $\omega \leq 0.1$ rad/s.

A similar analysis of the effect of the ramp strain can be done for the stress relaxation test. Experimentally, $\sigma_{ramp}(t)$ is measured but we assume this is $\sigma_{step}(t)$. This assumption leads to the same error function as described for the creep experiment (equation 2.18). The resulting approximation for the complex modulus ($E^*_A(\omega) = E'_A(\omega) + iE''_A(\omega)$) is given by:

$$E'_A(\omega) = E'(\omega)Er'(\omega) + E''(\omega)Er''(\omega) \tag{2.20a}$$

$$E''_A(\omega) = E'(\omega)Er''(\omega) + E''(\omega)Er'(\omega) \tag{2.20b}$$

By a similar analysis to that of the creep test, the effect of the ramp is small when $\omega = 0.1$ rad/s when $t_0 = 1$ s. Thus analysis for both experiments of the corresponding complex spectra is reasonable up to $\omega = 0.1$ rad/s. Evidence of this ramp associated error for both creep and stress relaxation experiments is found by comparison of processing $D^*(\omega)$ and $E^*(\omega)$ with both approaches 1 and 2 provided in section 4.1.3.

2.2.2 Approach 2

Processing using this approach uses all the experimental data including the ramp. Only frequency domain processing is considered here. $E^*(\omega)$ and $D^*(\omega)$ estimated from this approach are used for validation of these quantities estimated using approach 1 processing.

Approach 2: Creep

For approach 2, the effect of the ramp is not neglected when processing creep data. According to equation 2.3 it should be possible to calculate the frequency response $D^*(\omega)$ or $E^*(\omega)$ by simply taking the ratio of the Fourier transforms of the experimental stress and strain data. This procedure is essentially a deconvolution technique, which should remove the effect of the ramp leaving a true estimation of the spectrum of material properties. This technique has been cited to work by G. Zhang [42]. Unlike approach 1, this approach does not provide a simple Voigt model description of the $\varepsilon(t)$, therefore it is not possible to separate individual responses (eg. D_E, D_{VE}, D_L) as in approach 1.

Since experimental data is sampled discretely in time, it is necessary to calculate the discrete time Fourier transform of these signals; this is accomplished by taking the FFT (Fast Fourier Transform) of the signal. However, errors arise when calculating the FFT of a signal such as the unit ramp function used to generate the constant stress data in a creep test. For the creep test, the experimental strain data also follows this form once the linear term is removed. A technique has been developed by Nicolson [24] that provides a method for correcting for the error associated with taking the FFT of such signals. A detailed description of Nicolson's method can be found in appendix A.2.

Even though Nicolson's method requires removal of the linear term, it is still possible to obtain $E^*(\omega)$ (or $D^*(\omega)$) from all the $\varepsilon(t)$ and $\sigma(t)$ data. To accomplish this, the linear term must be added back to the data in the frequency domain via the superposition principle (see equations 2.21- 2.24). The linear term takes the form, βt for $t > 0$; where β is the slope and t is time. The Fourier transform of this linear term is $-\beta/\omega^2$.

$$D^*(\omega) = \frac{\tilde{\varepsilon}(\omega)}{\tilde{\sigma}(\omega)} = \frac{\mathfrak{F}\{\varepsilon(t)\}}{\mathfrak{F}\{\sigma(t)\}} \tag{2.21}$$

$$= \frac{\mathfrak{F}\{\varepsilon(t) - \beta t + \beta t\}}{\mathfrak{F}\{\sigma(t)\}} \tag{2.22}$$

$$= \frac{\mathfrak{F}\{\varepsilon(t) - \beta t\} + \mathfrak{F}\{\beta t\}}{\mathfrak{F}\{\sigma(t)\}} \tag{2.23}$$

$$= \frac{\mathfrak{F}\{\varepsilon(t) - \beta t\} + (-\beta/\omega^2)}{\mathfrak{F}\{\sigma(t)\}} \tag{2.24}$$

The step-by-step procedure for analyzing creep data using approach 2 can be found in the appendix A.1.3.

Since the Fourier transform of both strain and stress data from creep measurements can be accurately obtained by utilizing Nicolson's method and the superposition principle, $E^*(\omega)$ and

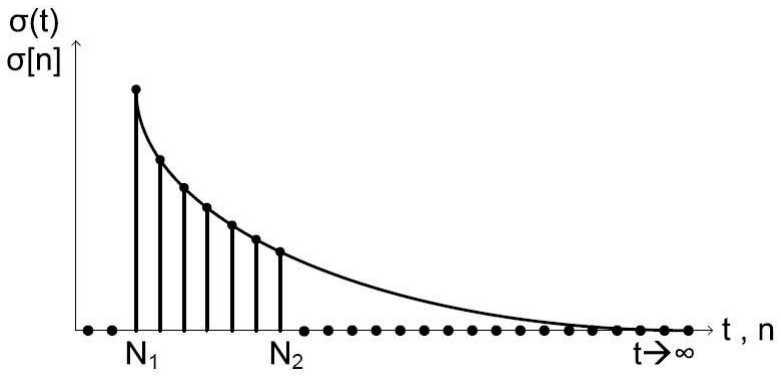

Figure 2.5: Discrete representation of stress relaxation data. The continuous line is the continuous time data $\sigma(t)$, and the stem plot is the discrete samples $\sigma[n]$ of $\sigma(t)$.

$D^*(\omega)$ found from approach 2 processing are good estimates of the frequency dependent material properties. Unlike approach 1, approach 2 is unaffected by the applied ramp stress, thus better estimates of the high frequency response are obtained.

Approach 2: Stress Relaxation

Approach 2 for stress relaxation data is not as reliable as it is for creep data. The reason for this is the limitation in the estimation of the FFT of time domain data that has not completely converged. Unfortunately, the typical time constants associated with gels such as those used in this study exhibit very long time constants outside the range of the 3600 s acquisition time used for stress relaxation experiments.

The experimental stress relaxation data takes the form of discretely sampled time domain data that has not completely converged over the data acquisition time. In order to obtain the frequency response of such a signal, the discrete-time Fourier transform is taken. Since the measured signal $\sigma(t)$ is discrete, it is more correct to describe it as $\sigma[n]$, where n represents the discrete points obtained over time. An illustration of this situation is seen in figure 2.5.

To take a discrete-time Fourier transform of $\sigma[n]$, the signal is assumed to be periodic, with $\sigma[n]$ representing a single period of length N, with the following Fourier series representation of the

periodic signal $\hat{\sigma}[n]$ (the following notation is based upon that used by Oppenheim et al. [25]):

$$\hat{\sigma}[n] = \sum_{b=<N>} a_b \exp(ib(2\pi/N)n), \text{ where} \tag{2.25}$$

$$a_b = \frac{1}{N} \sum_{n=<N>} \hat{\sigma}[n] \exp(-ib(2\pi/N)n) \tag{2.26}$$

$$= \frac{1}{N} \sum_{n=N_1}^{N_2} \sigma[n] \exp(-ib(2\pi/N)n) \tag{2.27}$$

$$= \frac{1}{N} \sum_{n=-\infty}^{\infty} \sigma[n] \exp(-ib(2\pi/N)n) \tag{2.28}$$

where $b =< N >$ indicates that b varies over the range of N successive integers.

Notice in Equation 2.28, the equality only holds if the discretely sampled data contains all the time information. Unfortunately, for the stress relaxation data, the discretely sampled data does not represent all time, thus the discrete time Fourier transform will only be an approximation. The more data obtained, the better the approximation.

There is no need for a detailed description of how to process data using this approach. The applied strain data is treated with Nicolson's method just as the applied stress data was for the creep experiment. The stress data is also treated with Nicolson's method under the assumption that data beyond the final acquisition point is constant. Unfortunately this is not the case, the data is not constant beyond the last acquisition point. However, the rate at which the stress changes at long times is much lower than that at short times, therefore application of Nicolson's method will provide a reasonable approximation. Approach 2 processing of stress relaxation data can be used for comparative and confirmative information, but it will not be used for reported spectral findings. If a deconvolution technique is desired for finding $D^*(\omega)$ or $E^*(\omega)$, I believe it is better to extract these responses from the creep data.

2.3 Summary

For time domain analysis of creep and stress relaxation measurements on gelatin hydrogel specimens, approach 1 processing is used to extract imaging parameters. Under approach 1, the applied stress or strain is assumed to be applied as a step function. This assumption allows the data to be well modeled by Voigt and Maxwell models. A low order ($K = 3$) Voigt model is applied to creep measurements on homogeneous gel samples and heterogeneous gel phantoms. This model provides estimates on ε_k, T_k, E_0, and β, which are all potential imaging parameters for pH. Stress relaxation

measurements on homogeneous gel samples provides an estimate of the E_0 imaging parameter.

The interpretation of pH sensitive imaging parameters estimated from time domain analysis can be aided by frequency domain analysis of the complex modulus. $E^*(\omega)$ provides separable frequency dependent information about the elastic (storage modulus $E'(\omega)$) and viscous (loss modulus $E''(\omega)$) components of the gel network. An estimate of $E^*(\omega)$ can be directly obtained from time domain $\varepsilon(t)$ or $\sigma(t)$ data from creep and stress relaxation measurements, respectively, under approach 1 processing. However, due to neglecting the effect of the ramp, large errors arise at frequencies greater than $\omega = 0.1$ rad/s.

Approach 2 processing of creep and stress relaxation measurements can be used to obtain estimates of $E^*(\omega)$ without neglecting the effect of the ramp. Thus, this method can be used to validate $E^*(\omega)$ estimates obtained via approach 1 processing.

For either approach, creep measurements provide better estimates of $E^*(\omega)$ than stress relaxation measurements. The reason for this is the creep measurements exhibit a linear response at long times that can be well modeled, extracted, and superimposed in the frequency domain. On the other hand, at long times, stress relaxation measurements have not completely converged, thus $E^*(\omega)$ estimates are more of an approximation than those obtained from creep measurements.

Chapter 3

Methods

In this chapter the sample preparation methods are described. Followed by a description of experimental methods for mechanical testing and elasticity imaging.

3.1 Hydrogel Specimens

The three different experiments performed on gelatin gels are illustrated in figure 3.1. For creep and stress relaxation measurements, samples of the same shape were used, however, the elasticity imaging experiment used gel blocks of a different shape and construction. To avoid confusion the gel specimens for creep and stress relaxation measurements are referred to as 'gel samples'; and gel specimens for elasticity imaging are referred to as 'gel phantoms'. We found that mechanical properties of these gels are extremely sensitive to slight variations in thermal history during production, storage, and experimentation. Effort was made to create gel specimens in which the conditions were similar in order to better relate the results across experiments; the commonalities are described here.

All gelatin gel specimens were constructed with 250 bloom strength, Type B gelatin provided by Rousselot (Dubuque, IA). Type B gelatin is obtained from animal hides by an alkali hydrolysis reaction. The IEP of the particular gelatin used in this study is known to be in the range 4.8-5.2. Gel specimens are comprised of 8% w/w gelatin, 91.9% w/w deionized water and 0.1% w/w formaldehyde. The formaldehyde is a 37% w/w solution, which contains 10-15% methanol as a preservative (Thermo Fisher Scientific, Waltham, MA). Under these conditions the pH of the hydrogel is 5.6. This pH is close to the IEP reported by the manufacturer. According to Hitchcock [19], the pH of the gel will approach the gelatin IEP as the gelatin concentration in water increases. From this point forward, pH 5.6 will be referred to as the IEP. The pH of the gels was lowered by adding a volume 1N HCl and raised using 1N NaOH as described below.

The gelatin and water were combined in a glass beaker, heated in a water bath at 60°C for 1 hour, and stirred every 10 minutes. Once the gelatin solution was removed from the heat, it was

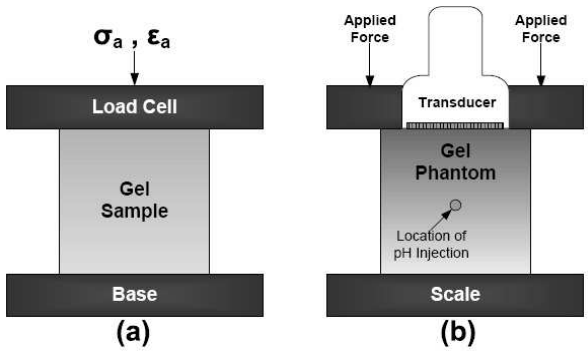

Figure 3.1: This figure displays schematics of the three experimental methods. **(a)** illustrates unconfined uniaxial compression (when the stimulus is stress this is a creep experiment, and when the stimulus is strain this is a stress relaxation experiment). **(b)** illustrates the elasticity imaging experiment.

allowed to cool at room temperature (21-22°C) to 50°C before adding formaldehyde. To prevent water loss, the beaker was covered with aluminum foil throughout the process. Further sample preparation varied between the two types of gel specimens as discussed below.

3.2 Gel Samples for Creep and Stress Relaxation Measurements

The purpose of creating homogenous gel samples at pH levels 4.6, 5.6, and 6.6 was to systematically study the mechanical properties of gelatin gels ±1 pH unit about the IEP. Creep measurements on these gels were used to determine pH sensitive contrast parameters. Stress relaxation measurements provided an alternative method for analyzing VE properties as a function of pH. Both measurements allowed estimation of $E^*(\omega)$ and associated VE parameters as a function of pH.

Gel samples constructed for the unconfined creep and stress relaxation tests were homogenous cylinders of height and diameter 44.5 mm. After preparing the gel solution as described in section 3.1, HCl or NaOH was added as necessary to the gelatin solution immediately following the addition of formaldehyde. The solution was then further cooled to 40°C before being poured into rigid plastic molds (see figure 3.2). Mold release (Pol-Ease 2300 by Polytek, Easton, PA) coats the inside of the mold to prevent adhesion of the gel with the plastic. The gel entered the mold by pouring the warm solution through the 3cc Leur-Lok syringe located at the top of the apparatus. There is a release hole (not displayed in figure 3.2) drilled into the side of the syringe about 2.5 cm above the base of the syringe. Gel was filled just beyond this release hole. The piston of the Leur-Lok syringe was

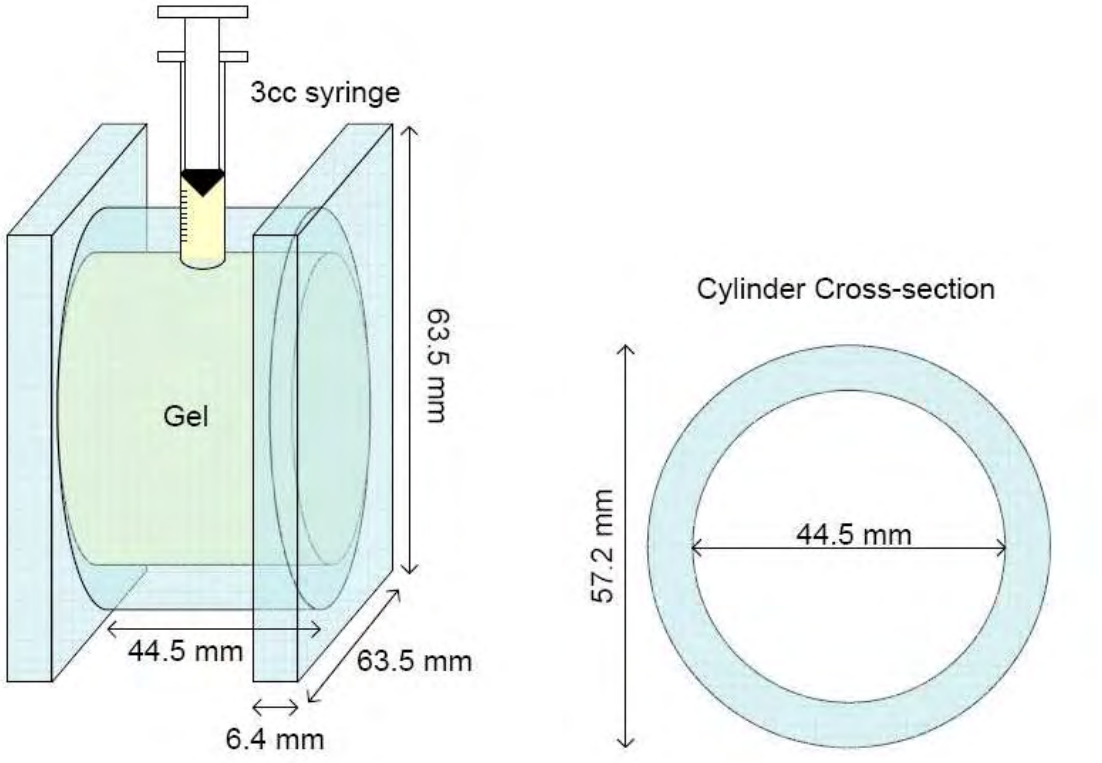

Figure 3.2: The figure on the left is a schematic of the plastic mold used for creating unconfined gels. The mold consists of two flat acrylic plates and one piece of cylindrical acrylic tubing. A C-clamp (not shown) is used to hold the acrylic tubing and flat acrylic plates together. A 3cc Leur-Lok syringe (with its tip removed) is positioned in the top of the tubing. The syringe is positioned perpendicular to the tubing and parallel to the plates to allow any air pockets to escape to the syringe. The figure on the right displays a cross-section of the acrylic tubing.

then inserted into the barrel of the syringe until all excess gel was expelled from the release hole. The gel was then allowed to cool to room temperature. Care must be taken to assure air bubbles do not form in the gel as it cools in the molds. Ideally, if bubbles form in the sample, because of the positioning of the overfilled syringe, they will travel up the barrel of the syringe and displace the excess gel. However, due to the slightest experimental error in alignment of the syringe, the bubbles must often be coaxed to move towards the barrel of the syringe by agitating the sample slightly.

The total polymerization time (t_p) is considered to be the time from which the gel is allowed to start cooling until the time the sample is tested. For these gels, $t_p = 48$ hours at room temperature. The quantities of HCl and NaOH necessary to shift the gelatin solution pH were empirically determined and are displayed in table 3.1. Based upon these findings, an asymmetric relationship is observed about the IEP in regard to the number of H^+ and OH^- ions needed to shift the pH.

Table 3.1: The fraction by total sample weight of acid (1N HCl) or base (1N NaOH) that was added to gel solutions to achieve stated pH values. The specific gravity of the 1N HCl and 1N NaOH solutions is approximately 1.

pH	**4.1**	**4.6**	**5.1**	**5.6**	**6.1**	**6.6**	**7.1**
HCl w/w%	3.0	1.56	0.69	0	0	0	0
NaOH w/w%	0	0	0	0	0.31	0.56	0.75

This observation is in agreement with previous studies of Type B gelatin [39].

3.3 Gel Phantoms for Elasticity Imaging Measurements

The purpose of this elasticity imaging study was to detect VE contrast due to spatial variations in gel pH in an otherwise homogeneous phantom. This was accomplished by creating a linear track at the center of a gel cube that was allowed to polymerize in the presence of an acid or a base. Introduction of a localized pH change in the gel solution before polymerization to the gel state is intended to simulate changes in breast tissue stroma near acidic tumors.

Imaging phantoms were constructed using the gelatin solution as described in section 3.1. After the formaldehyde was added, the gelatin solution continued to cool at room temperature to 45°C after which 3.35% w/w graphite was mixed thoroughly with a spoon. When the gel temperature reached 40°C, the still molten solution was placed into a vacuum chamber for < 5 minutes to remove gasses introduced by the graphite suspension process. The solution was then poured into a mold and cooled at room temperature. The inside surfaces of a 50-mm cubic phantom mold case were coated with mold release, and one piece of PE-50 tubing (OD: 0.965 mm, ID: 0.58 mm) was inserted through the center of opposing sides of the acrylic mold as illustrated in figure 3.3. The warm gel solution was poured into the mold through the 10cc syringe. The syringe was closed by inserting a thin wire down the inside wall of the syringe while pushing the syringe piston down to the level of the gel. Once the syringe piston was in contact with the gel, the wire was slowly removed. This procedure resulted in an air tight seal without any bubbles. It is important to avoid bubbles in the ultrasound phantoms because air bubbles will attenuate the ultrasound signal. Silicone was used to seal all temporary joints including the intersection between the phantom mold and tubing. The phantom mold apparatus was attached to a rotation table using a 4" C-clamp and rotated at 1 rpm for approximately 2 hours to prevent graphite settling as the gelatin solution polymerized.

Graphite was added to these phantoms to provide ultrasonic tissue-like scattering and absorption.

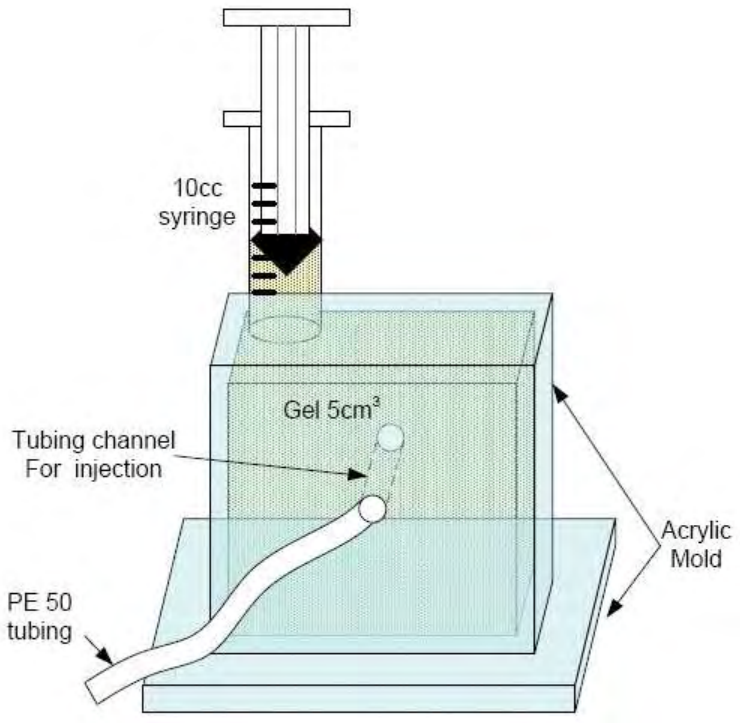

Figure 3.3: Schematic of the mold used for creating elasticity imaging gel phantoms. A 4 inch C-clamp is used to hold the acrylic mold to the rotation table (not shown). A 10cc Leur-Lok syringe (with its tip removed) is positioned in the top of the mold for gel entry.

In comparison with the creep and stress relaxation samples, we assume the effect of graphite on the gel mechanical properties is small. According to Hall et al. [17] graphite produces a small effect on gel stiffness giving an elastic modulus difference on the order of 1 kPa between a phantom with and without graphite at 5.5%w/w concentration.

After approximately 2 hours of rotation, the gelatin solution was a very weakly polymerized gel. Fluids could freely diffuse in the highly viscous medium. At that time the acid or base was infused very slowly into the PE-50 tubing while the tube was slowly withdrawn from the case at a relatively constant rate. This was accomplished by using a syringe connected to a syringe pump with a 27 gauge needle inserted into the tubing. The back of the needle was attached to the tubing using hot glue; this prevented any fluids from escaping the tubing during injection. The syringe pump allows the injection fluid to flow through the tubing at a flow rate of 0.5 ml/min. As the fluid was flowing through the tubing, the tubing was simultaneously pulled through the gel phantom leaving a channel of fluid in its path. Once the injection was complete, the case exit holes were sealed with hot glue. The goal was to leave a uniform linear path of acid or base that could quickly diffuse without also leaving a structural defect in the gel once it had fully congealed. After injection, the phantom quiescently congealed at room temperature for 48 hours before measurement. Three phantoms were constructed: an acidic injection of 1N HCl, a control injection of deionized water mixed with HCl to have a pH of 5.6, and a basic injection of 1N NaOH. Clinically we do not expect basic conditions, these phantoms were constructed for completeness of this pH study and for validation of our results with those presented in literature.

3.4 Creep and Stress Relaxation Measurements

Creep and stress relaxation measurements were performed on the gel samples described in section 3.2 using a TA.XT Plus Texture Analyzer System and a 1kg load cell (Texture Technologies Corp., Scarsdale, NY). Displacement and force data were acquired at 10 samples/second. Strain is found from the displacement data based upon the initial height of the sample after the pre-load was applied. Stress is found from the the force data using the initial cross-sectional area of the gel specimen. The initial diameter of the specimen is 44.5 mm (see section 3.2). The top and bottom of the gel samples were coated with a thin layer of oil to provide free-slip conditions and minimize desiccation. The gels were compressed using a 3 inch diameter flat aluminum plate. An acrylic environmental box enclosed the analyzer system (as seen in figure 3.4) to stabilize temperature and minimize air flow

Figure 3.4: Photograph of the TA.XT with the acrylic environment box surrounding it.

around the samples. We observed that the gel internal temperature dropped approximately 5°C over the testing time of 1 hour when the environment box was not used. When using the environment box there is a temperature gradient as well; the TA.XT generates heat during operation causing the temperature of the environment to increase by a maximum of 3°C above room temperature. But when the environment box was utilized the temperature of the gels maintained an internal temperature within 1°C of the room temperature. Thus, the testing conditions of the gel specimens are more stable when using the environment box.

To determine the linear stress-strain range of the gel samples, a 30 g pre-load (∼2% strain) followed by a cyclic triangular-wave pattern of loading and unloading an additional 10% strain at a period of 25 s was applied to the samples (figure 3.5). These tests were performed using the analyzer system. A pre-load was applied to minimize tensile forces between the compression plate and the sample during the unloading portion of the cycle. The pre-load also minimized displacement uncertainty due to loss in sample height. Analysis of the stress versus time data suggests that the transient effects of the gels are minimal after about 35 cycles, and the loading curve is approximately linear over the range of 10% engineering strain (figure 3.5). Taking the slope of the loading portion

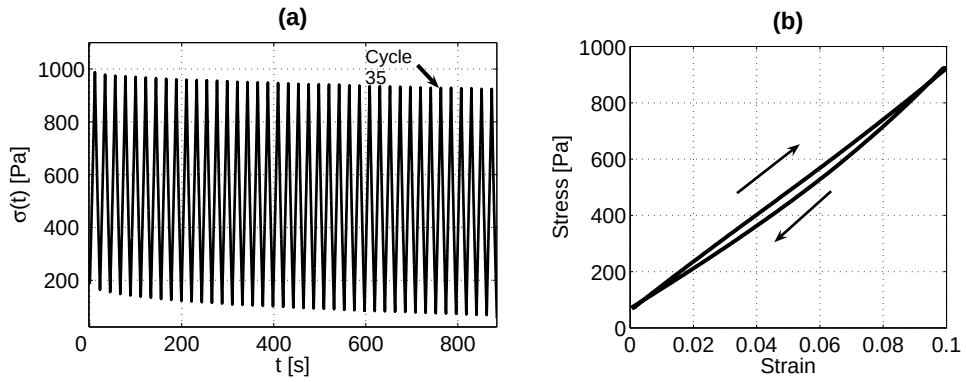

Figure 3.5: The stress versus time plot **(a)** of the stress-strain preconditioning on an IEP gel (pH 5.6) for 40 cycles. Figure **(b)** displays cycle 40 of the stress-strain data used to estimate E_0.

of the 40th stress-strain curve provides an estimation of the elastic modulus (E_0) for each sample. Because of the transient response of the gel samples, this procedure was used to precondition all gel samples immediately before creep or stress relaxation measurements.

Creep curves were measured by applying a uniaxial stress of $\sigma_a = 720$ Pa to samples, while stress relaxation curves were recorded by applying a uniaxial strain of $\varepsilon_a = 0.08$. In both cases a 15 g preload ($\sim$1% strain) was applied to ensure good contact between the compression plate and sample. For both experiments, the stimulus was applied during a ramp of approximately 1 second and held constant for 3600 seconds. The output strain or stress data is processed under the assumption of a step input by shifting the first point of the output after the ramp to time = 0 seconds (approach 1). The ramp data was disregarded. This approximation has a minor impact on the spectral response up to $\omega = 10^{-1}$ rad/s as described in sections 2.2.1 and 4.1.3. Under this assumption the initial elastic response of each of these experiments provides an additional estimation of E_0.

3.5 Elasticity Imaging Measurements

Strain imaging experiments were performed on the pH injection phantoms described in section 3.3 in the form of an unconfined uniaxial creep test as described elsewhere [35]. The bottom surface of the phantom was coated in oil to simulate free-slip boundary conditions, and the top surface was coated with an acoustic coupling gel. A flat plate that holds the ultrasonic transducer was attached to a motion controller. The motion controller was programmed to ramp up to the applied stress level (between 850-900 Pa) in 1 second and was held constant for 1800 seconds. A uniaxial stress was applied in the direction of the sound beam and normal to the top surface of the sample, which

was placed on a fixed-height digital scale. The scale provides feedback to the motion controller of the measured stress in order to maintain the appropriate displacement to achieve constant stress.

RF echo data were acquired by a Siemens Sonoline-Antares system with the Ultrasound Research Interface (URI) feature and a VF10-5 linear array transducer transmitting at 8 MHz. The RF frame rate was controlled through a waveform generator (Wavetek 30Ms/s Universal Waveform Generator Model 39) connected to the ECG trigger input. The waveform generator output a square wave signal with an amplitude of 50 mV peak-to-peak. Data were acquired at 4 frames per second for the first 80 seconds and then at 2 frames per second for the final 1720 seconds. The initial acquisition rate is sufficient to capture the initial elastic response and short duration viscoelastic responses. A pre-load strain of approximately 2-3% was applied to the phantom to ensure good acoustic contact with the transducer. Strain images were generated using the multi-resolution cross correlation algorithm [4].

3.6 pH Indicator Gels

An independent experiment using pH indicator solution (Universal pH indicator system from Thermo Fisher Scientific, Waltham, MA) was performed as a way to independently assess the pH of the gel visually by color contrast. This study was used to both validate that changes in viscoelastic properties were related to pH changes and to aid in the identification of the true pH distribution in the phantoms. Gelatin gels were manufactured according to the general procedure described in section 3.1. A set of gel samples were created by systematically changing the pH to 4.6, 5.6, and 6.6. Immediately following the addition of HCl or NaOH, 1%w/w pH indicator was added; the samples were thoroughly mixed and color photographs were taken with a digital camera at $t_p = 48$ hours. From the image data, a color was assigned to each pH level.

A version of the elasticity imaging phantoms with HCl and NaOH injections were also created. The phantoms were prepared as described in section 3.3 except pH indicator solution (1%w/w) was added after the formaldehyde and graphite was omitted. After the HCl or NaOH was injected, the spatial variation in pH was tracked by observing color variations. Photographs of these gels were taken at $t_p = 48$ hours.

Chapter 4

Results

In this chapter, time and frequency domain results of creep and stress relaxation measurements on gel samples are discussed. Imaging parameters estimated from these experiments are described. Finally, the elasticity imaging results are analyzed and the sensitivity to pH imaging is assessed.

4.1 Results of Creep and Stress Relaxation Measurements

Time and frequency domain methods were applied to creep and stress relaxation measurements of gel samples to estimate and interpret VE parameters with pH. At each pH level (pH 4.6, 5.6, and 6.6) 4 gelatin gel samples were created from a single batch; two samples were used for creep and two for stress relaxation. The room temperature from the time of sample construction until measurement did not vary more than $1°C$. In this section, we describe the results obtained via these methods as well as a discussion of sources of experimental error.

4.1.1 Time Domain

Representative creep curves for gel samples at pH 4.6, 5.6, and 6.6 are displayed in figure 4.1a. To find pH sensitive parameters, we fit the creep data to a tri-exponential Voigt model (see figure 4.1b) using approach 1 processing (described in section 2.2.1). To be consistent with the acquisition time of the elasticity imaging measurements, we only used the first 1800 seconds of creep data for curve fitting.

Based upon curve fitting results, it is clear that strain amplitudes decrease with pH, which corresponds to an increase in the elastic response with pH. However this response is asymmetric about the IEP. Also, the strain amplitudes (ε_0, ε_1, ε_2) and β are much more sensitive to pH than the VE time constants (T_1, T_2). Even though there are only two samples at each pH, similar results have been obtained in a previous investigation [41]. Since pH variations in hydrogels was found primarily in the strain amplitudes and β, it is reasonable to focus the analysis of pH effects on ε_0

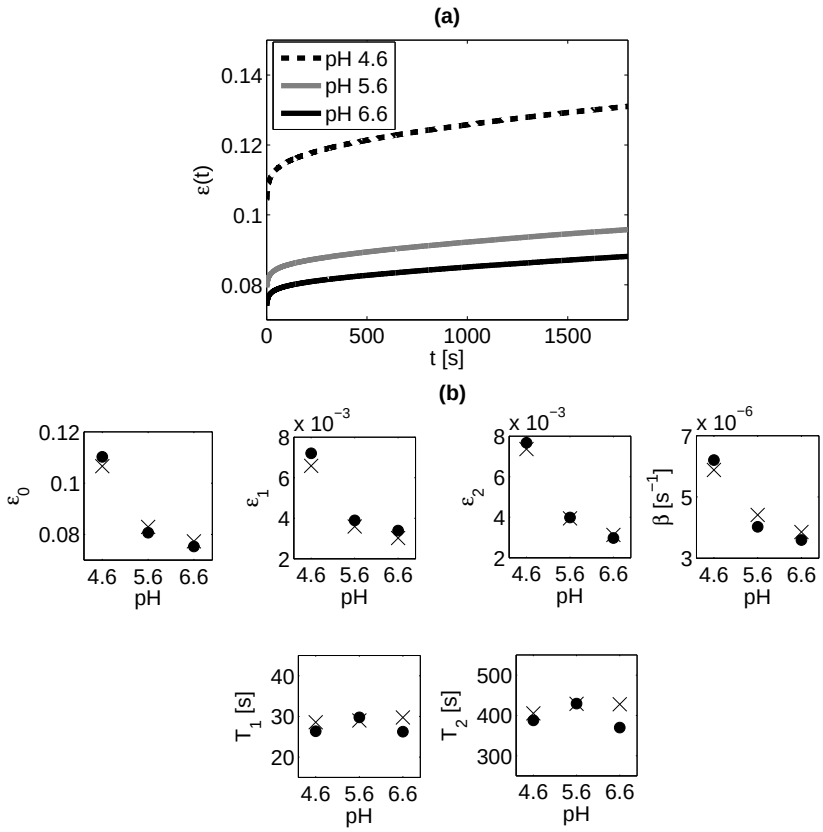

Figure 4.1: **(a)**: Strain data for representative creep experiments on gel samples at pH 4.6, 5.6, and 6.6. **(b)** row 1 provides the strain amplitude parameters and β for a tri-exponential Voigt model. **(b)** row 2 provides the VE time constants of the model. Results of two gel samples are displayed for each pH level with $\bullet$ corresponding to sample 1 and $\times$ corresponding to sample 2.

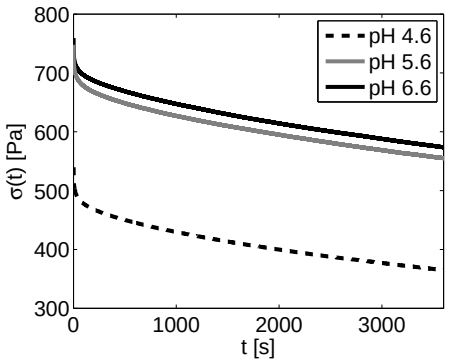

Figure 4.2: Stress data for representative stress relaxation experiments on gel samples at pH 4.6, 5.6, and 6.6.

and β. Further analysis of the other exponential amplitude components is neglected because their amplitudes are approximately 2 orders of magnitude smaller than the ε_0 amplitude for gelatin gels and therefore measurements of ε_1 and ε_2 have much higher percent errors than for ε_0. β is chosen for further analysis as well because it represents contrast evident at longer measurement times.

The time domain results of representative stress relaxation data for different pH gels 4.6, 5.6, and 6.6 are processed according to approach 1 (see section 2.2.1) and are displayed in figure 4.2. It is evident from the $\sigma(t)$ results that the initial elastic response ($\sigma(t=0)=\sigma_0$) of the gel samples increases with pH in an asymmetric fashion about the IEP similar to that observed from the creep data.

As discussed in section 3.4 stress-strain preconditioning was performed on all gel samples prior to creep or stress relaxation measurements. This preconditioning provided a measurement of E_0 for each of the 4 gel samples at each pH level. These results are summarized in table 4.1 where $\bar{E_0}$ is the average modulus measurement of the 4 samples and SD is the sample standard deviation. E_0 was also estimated from the initial elastic response ε_0 and σ_0 of the creep and stress relaxation time domain measurements using approach 1 (see section 2.2.1), respectively. Thus we have 3 methods for estimating E_0 for each pH level. Because of systematic error due to thermal history (discussed in section 4.1.4) it is more useful to compare ratios of E_0 with respect to pH 5.6 in order to focus on contrast due to pH changes rather than sample variations. We define a parameter $E_{CR} = \frac{\bar{E_0}|_{pH}}{\bar{E_0}|_{pH=5.6}}$ to describe these ratios. The E_{CR} values corresponding to $\bar{E_0}$ measurements from stress-strain preconditioning, creep, and stress relaxation measurements on gel samples are displayed in figure 4.3a. A similar ratio approach is taken for analysis of the β parameter determined from creep measurements. We define $\beta_{CR} = \frac{\beta|_{pH}}{\beta|_{pH=5.6}}$ for this purpose and plot results in figure 4.3b. E_{CR}

Table 4.1: Average modulus $\bar{E}_0$ from stress-strain preconditioning measurements for $t_p = 48$ hours for the batches of gel stated. SD is the sample standard deviation.

Batch	$\mathbf{E_0}$ **[kPa]**	**SD [kPa]**	$\mathbf{SD/E_0\%}$
pH 4.6	6.17	0.135	2
pH 5.6	8.33	0.167	2
pH 6.6	8.91	0.208	2

Table 4.2: Average modulus $\bar{E}_0$ from stress-strain preconditioning measurements for $t_p = 9$ days for the batches of gel stated. SD is the sample standard deviation.

Batch	$\mathbf{E_0}$ **[kPa]**	**SD [kPa]**	$\mathbf{SD/E_0\%}$
pH 4.6	10.75	0.127	1
pH 5.6	13.68	0.098	1
pH 6.6	14.64	0.106	1

and β_{CR}^{-1} are ratios that describe quantities that are inversely proportional to a strain amplitude. The time domain creep and stress relaxation measurements on gel samples provide two potentially pH sensitive imaging parameters, E_{CR} and β_{CR}^{-1}. E_{CR} describes changes in the elastic modulus due to variation in instantaneous strain. While β_{CR}^{-1} describes long time changes in the elastic response.

Figure 4.4 illustrates the small error associated with estimating E_0 from creep and stress relaxation data using approach 1 processing. The average elastic modulus estimate from the creep and stress relaxation measurements $\bar{E}_0$ is compared with the average elastic modulus measured from the stress-strain preconditioning. The stress-strain preconditioning estimate of $\bar{E}_0$ is estimated without ignoring data, thus we believe this is good estimate of the true modulus of the gels. The estimates from creep and stress relaxation measurements processed according to approach 1 show little variation from the true estimate.

4.1.2 Frequency Domain: Approach 1

Creep and stress relaxation measurements on gel samples provide independent estimates of $E^*(\omega)$ as described in chapter 2. For this frequency domain analysis, the full 3600 s of data was used to maximize the frequency bandwidth. Representative storage $E'(\omega)$ and loss $E''(\omega)$ modulus spectra for pH levels 4.6, 5.6, and 6.6 for both creep and stress relaxation data are displayed in figure 4.5. In both cases, approach 1 processing was used (case **a** approach 1 for creep data). Analysis of $E^*(\omega)$ spectra show that the storage modulus is much more sensitive to pH changes than the loss modulus, which is consistent with time domain analysis (figure 4.1).

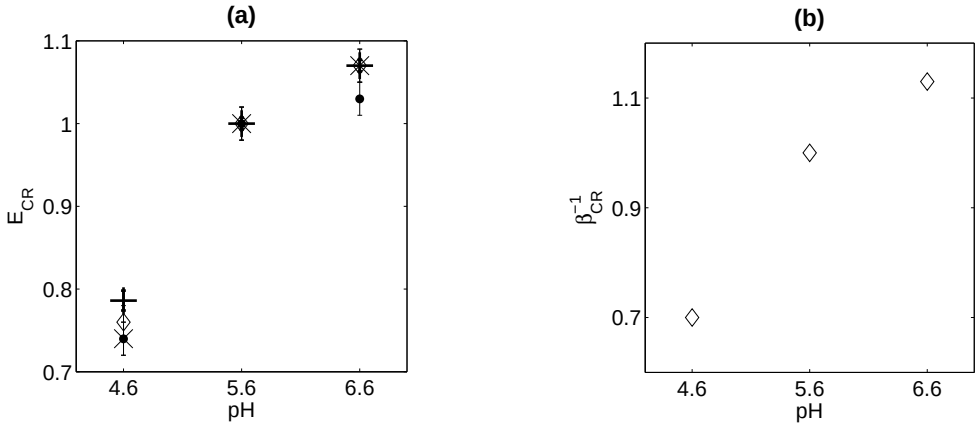

Figure 4.3: **(a)** displays E_{CR} values for $\bar{E}_0$ values for stress-strain preconditioning ($\times$) for t_p = 48 hours, creep ($\diamond$), and stress relaxation ($\bullet$) measurements for t_p = 48 hours, and stress-strain preconditioning ($+$) for t_p = 9 days. The error bars on $\times$ and $+$ data correspond to the $SD/\bar{E}_0$ values displayed in tables 4.1 and 4.2 respectively. **(b)** displays β_{CR}^{-1} calculated from average β estimates from creep measurements for $t_p = 48$ hours.

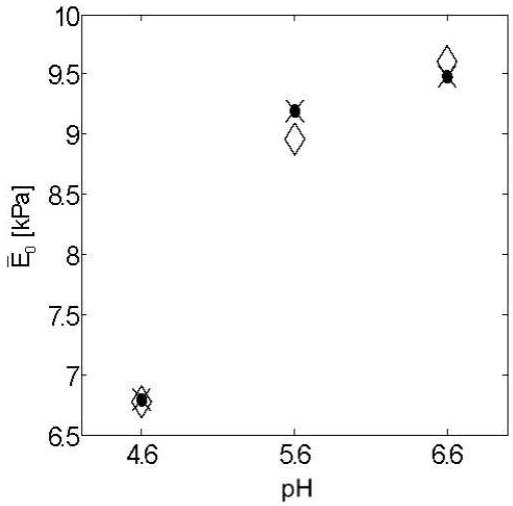

Figure 4.4: The small error associated with approach 1 processing of creep ($\diamond$) and stress relaxation ($\bullet$) measurements of gel samples is illustrated in terms of the $\bar{E}_0$ estimated from the IER, in comparison to the $\bar{E}_0$ measurements from the stress-strain preconditioning ($\times$).

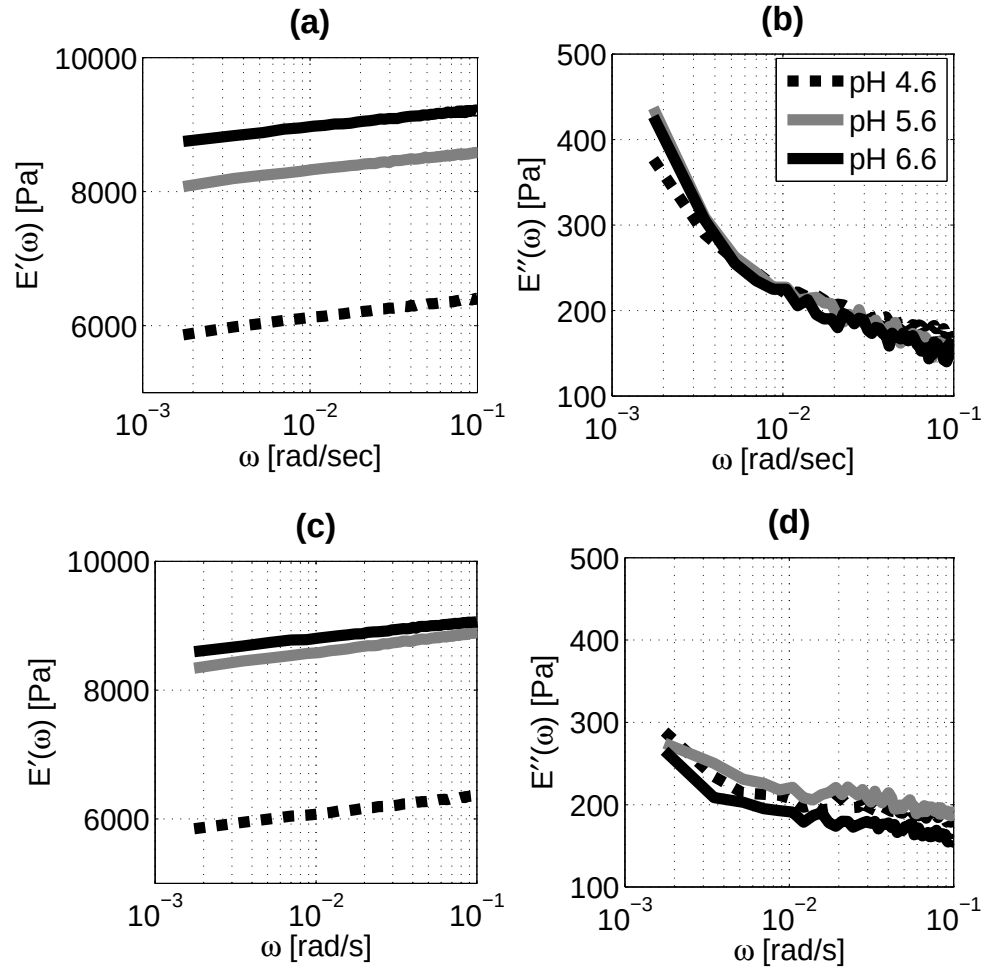

Figure 4.5: **(a)** and **(b)** display the storage $E'(\omega)$ and loss $E''(\omega)$ modulus spectra, respectively, for gelatin gels of pH 4.6, 5.6, and 6.6 as found from creep measurements. **(c)** and **(d)** display the same spectra as found from stress relaxation measurements. In both cases, approach 1 processing was used.

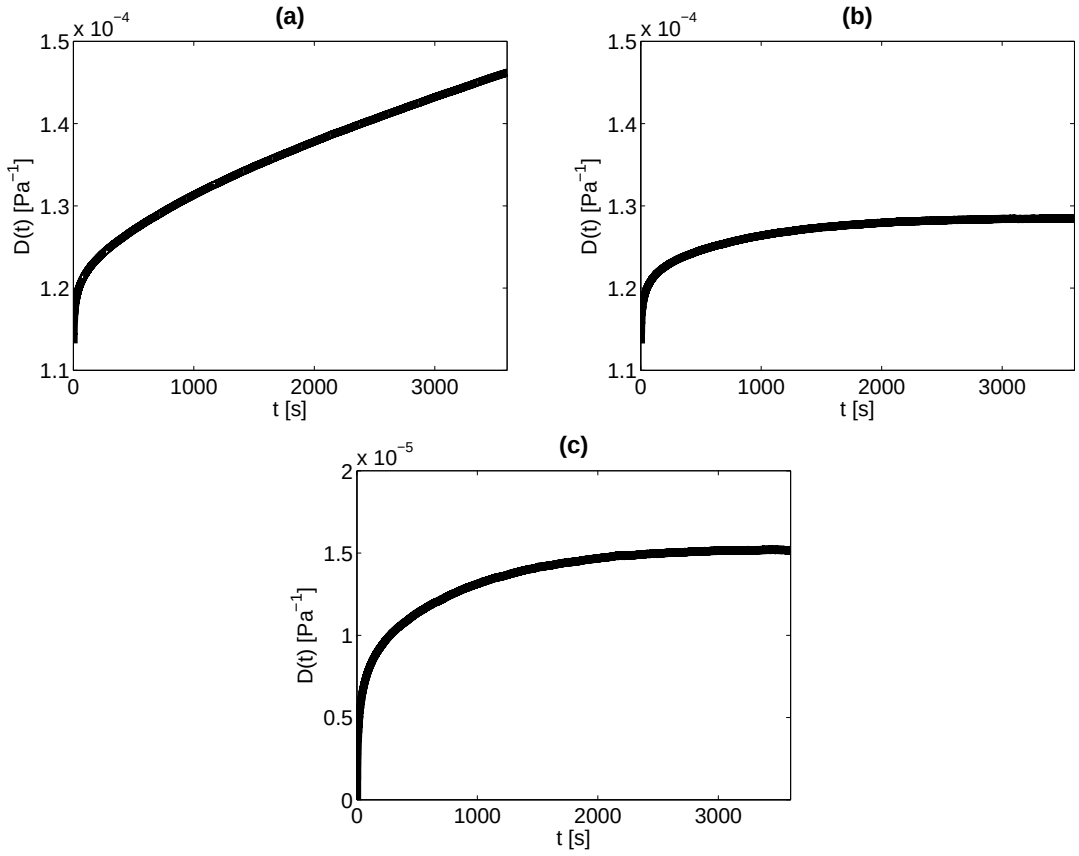

Figure 4.6: This figure displays the representative $D(t)$ data for creep measurements on gel samples represented in 3 ways corresponding to cases **a**, **b**, and **c** described in section 2.2.1 in figures **(a)**, **(b)**, and **(c)** respectively.

As noted in section 2.2.1, the compliance data from creep measurements can be separated into 3 components: elastic ($D_E(t)$), viscoelastic ($D_{VE}(t)$), and linear ($D_L(t)$). There are three ways of processing this data that is of interest (see cases **a-c** in section 2.2.1) for obtaining estimates of $E^*(\omega)$. For case **a**, we are interested in all three components ($D(t) = D_E(t) + D_{VE}(t) + D_L(t)$), these $E^*(\omega)$ results were displayed in figure 4.5a. For case **b**, we are interested in only the elastic and viscoelastic components ($D(t) = D_E(t) + D_{VE}(t)$). And for case **c**, we are interested in only the viscoelastic component ($D(t) = D_{VE}(t)$). An example of the time domain representation $D(t)$ for each of the three cases is displayed in figure 4.6a-c. At each pH level (4.6, 5.6, 6.6), a representative $E^*(\omega)$ spectra in terms of its storage ($E'(\omega)$) and loss ($E''(\omega)$) spectra is displayed for cases **b** and **c** in figures 4.7a,b and 4.7c,d respectively.

By comparison of the $E^*(\omega)$ response of cases **a-c**, it is clear that the elastic component $D_E(t)$ dominates the behavior of $E^*(\omega)$. When this term is present, the storage and loss modulus behavior

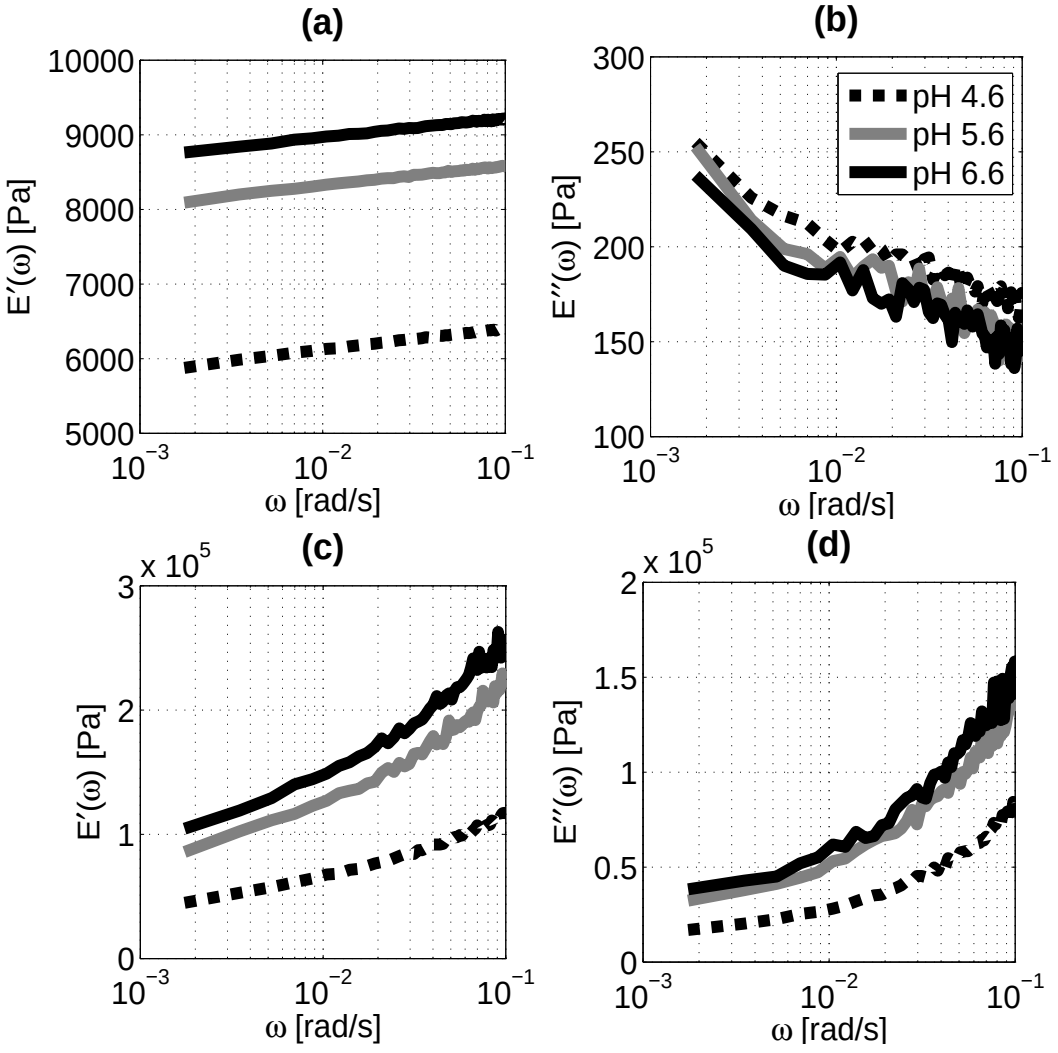

Figure 4.7: Figures **(a)** and **(b)** display the storage ($E'(\omega)$) and loss ($E''(\omega)$) spectra respectively for case **b** approach 1 processing of creep measurement data on gel samples for pH value 4.6, 5.6, and 6.6. Figures **(c)** and **(d)** display the similar spectra for case **c**.

is similar regardless of the linear component $D_L(t)$. However, when $D_E(t)$ is removed, the behavior of $E^*(\omega)$ changes. This strong effect of the elastic component is in agreement with the contrast findings for creep measurements. The linear component does effect the loss modulus at low frequencies. Interestingly, the case **b** $E^*(\omega)$ spectra from creep measurements (figure 4.7a,b) is more similar to the $E^*(\omega)$ spectra from stress relaxation measurements (figure 4.5c,d) than the case **a** spectra (figure 4.5a,b). This similarity is likely the result of the $E^*(\omega)$ processing complications with a signal that has not completely converged over the acquisition time such as the stress relaxation measurements in this study (see section 2.2.2). Since the $D_L(t)$ component of the creep data is likely due to a long time viscoelastic element, it is likely that a sufficient amount of data was not collected for the stress relaxation experiment to capture this long time response.

A simulation of creep and stress relaxation data confirms this conjecture regarding $E^*(\omega)$ processing complications from stress relaxation data. A simple Voigt model of creep data is given by the mono-exponential function

$$D(t) = D_0 + D_1\left(1 - \exp\left(-\frac{t}{T_1}\right)\right) + \frac{\beta}{\sigma_a}t \text{ , for } t > 0 \tag{4.1}$$

with corresponding $E^*(\omega)$

$$E^*(\omega) = \frac{1}{D^*(\omega)} = \frac{1}{D_0 + \frac{D_1}{1+i\omega T_1} + \frac{\beta}{i\omega\sigma_a}} \tag{4.2}$$

Equations 4.1 and 4.2 take the form of a standard linear liquid (SLL) [37], which is essentially a viscoelastic model that possesses a purely viscous response modeled by the linear component $\beta t/\sigma_a$ in this case. As mentioned in section 2.2.1, we do not believe this linear component represents a purely viscous response, but rather a long term VE element. However, over the experimental acquisition time, the material response is well modeled with the SLL model. For creep experiments, the SLL Voigt model consists of 2 elastic spring elements with compliance D_0 and D_1, and two viscous dashpot elements with viscosity coefficients η_1 and η_0 as displayed in figure 4.8a. The VE Voigt element consisting of D_1 and η_1 has a relaxation time $T_1 = D_1\eta_1$. Also, the linear term can be re-expressed as $\beta/\sigma_a = 1/\eta_0$ for the purpose of the SLL model. In order to chose an appropriate conjugate model for stress relaxation, we follow Alfrey's rules, which state [37]:

1. The number of elements of each kind (elastic and viscous) must be the same in the conjugate model.

2. A parallel combination of two elements of different kind is replaced by a series combination and vice versa.

3. The absence (presence) of an isolated element of one kind requires the presence (absence) of an isolated element of the other kind in the conjugate model.

Using Alfrey's rules and the assumption of a SLL model, the corresponding conjugate model for stress relaxation is illustrated in figure 4.8b and given by the following Maxwell model:

$$E(t) = E_1 \exp\left(-\frac{t}{\tau_1}\right) + E_2 \exp\left(-\frac{t}{\tau_2}\right) \tag{4.3}$$

with corresponding $E^*(\omega)$

$$E^*(\omega) = \frac{E_1 i\omega\tau_1}{1 + i\omega\tau_1} + \frac{E_2 i\omega\tau_2}{1 + i\omega\tau_2} \tag{4.4}$$

The Maxwell model contains the same number of springs and dashpots as the Voigt model, however, there are no stand-alone elements in this model. The time constants of equation 4.3 are related to the VE elements as $\tau_{1,2} = \eta_{M1,M2}/{E_{1,2}}^3$. The relationship between the Voigt and Maxwell SLL elements can be found by using the relationship $D^*(\omega)E^*(\omega) = 1$. According to Tschogel, this can be solved by using the Laplace domain variable s in place of $i\omega$. The first step is to substitute equations 4.2 and 4.4 into $D^*(\omega)E^*(\omega) = 1$. Then multiply both sides by the denominator and equate coefficients of s. According to Tschoegl [37], the parameters of equations 4.1 and 4.3 are related by the following

$$D_0 = \frac{1}{E_1 + E_2} \tag{4.5}$$

$$D_1 = \frac{(E_1E_2\tau_2 - E_1E_2\tau_1)^2}{E_1E_2(E_1 + E_2)(E_1\tau_1 + E_2\tau_2)^2} \tag{4.6}$$

$$T_1 = \frac{1/E_1 + 1/E_2}{1/(E_1\tau_1) + 1/(E_2\tau_2)} \tag{4.7}$$

$$\beta/\sigma_a = \frac{1}{E_1\tau_1 + E_2\tau_2} \tag{4.8}$$

The values of parameters used in this model are presented in table 4.3.

Since the parameters for these conjugate models are known, the analytic $E^*(\omega)$ spectrum can be obtained and compared to $E^*(\omega)$ estimated via approach 1 processing on both the simulated creep and stress relaxation data. To illustrate the effect of acquisition time on $E^*(\omega)$ processing of stress relaxation data, two acquisition times are considered: a short time of 1800 s, and a long time of

[3]Note that the time constants in the conjugate models are not equivalent, e.g. $\tau_{1,2} \neq T_1$

Table 4.3: Parameters for the simple Maxwell model used to simulate stress relaxation and creep data.

$\mathbf{E_1}$ [Pa]	$\mathbf{E_2}$ [Pa]	$\tau_\mathbf{1}$ [s]	$\tau_\mathbf{2}$ [s]
500	10100	100	1900

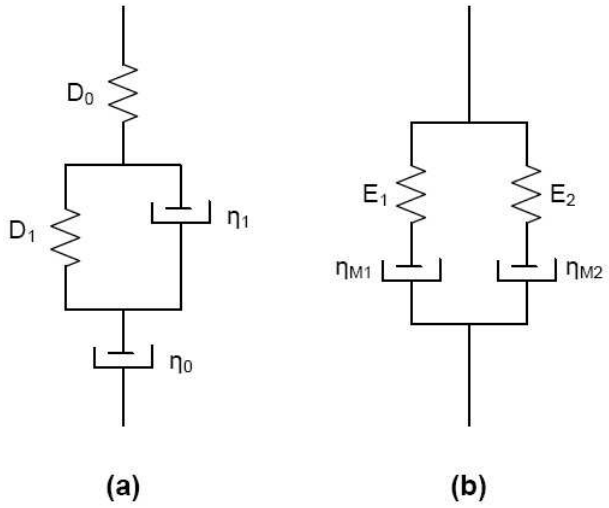

Figure 4.8: **(a)** represents the SLL Voigt model and **(b)** represents the conjugate SLL Maxwell model.

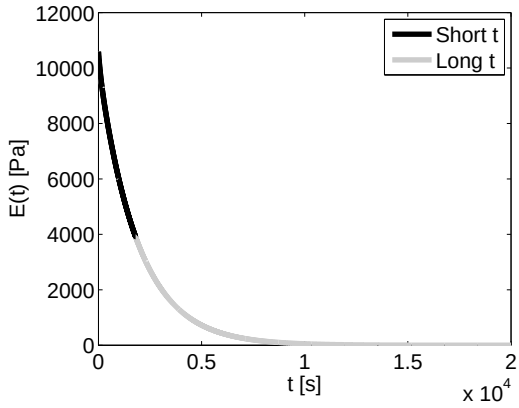

Figure 4.9: Model of stress relaxation data for a short acquisition time of 1800 s and a long acquisition time of 20000 s.

20000 s. It is evident from figure 4.9 that the long time acquisition exhibits fully relaxed $E(t)$ data, while the short time acquisition has not yet converged.

Applying approach 1 processing to both acquisition times of stress relaxation data indicates that the short time acquisition is not as good an estimate as the long time acquisition of $E^*(\omega)$ as illustrated in figure 4.10a,b. On the other hand, the short time acquisition of creep data processed using approach 1 is a good estimate of $E^*(\omega)$ (see figure 4.10c,d) provided the VE time constants are less than the acquisition time.

4.1.3 Frequency Domain: Approach 2

Analysis of the complex modulus $E^*(\omega)$ and complex compliance $D^*(\omega)$ spectra of creep and stress relaxation measurements via approach 2 processing, validates the spectra estimates obtained from approach 1 processing. Recall that the main difference between approaches 1 and 2 is that the ramp data is either ignored or included, respectively. Since approach 2 processing does not neglect the ramp, the error associated with approach 1 at high frequencies (see section 2.2.1) will not be a factor. In figure 4.11a-d, a representative creep measurement was processed using approach 1 case **a** to obtain an estimate of $E^*(\omega)$ and $D^*(\omega)$, the corresponding spectra processed according to approach 2 is also displayed. In figure 4.12a-d, a representative stress relaxation measurement was processed using approach 1 to obtain an estimate of $E^*(\omega)$ and $D^*(\omega)$, the corresponding spectra processed according to approach 2 is also displayed. For both creep and stress relaxation measurements, it is evident that the approach 1 processing is a good estimate at low frequencies, but as the frequency increases, the estimate weakens. This weakening is more evident in the loss

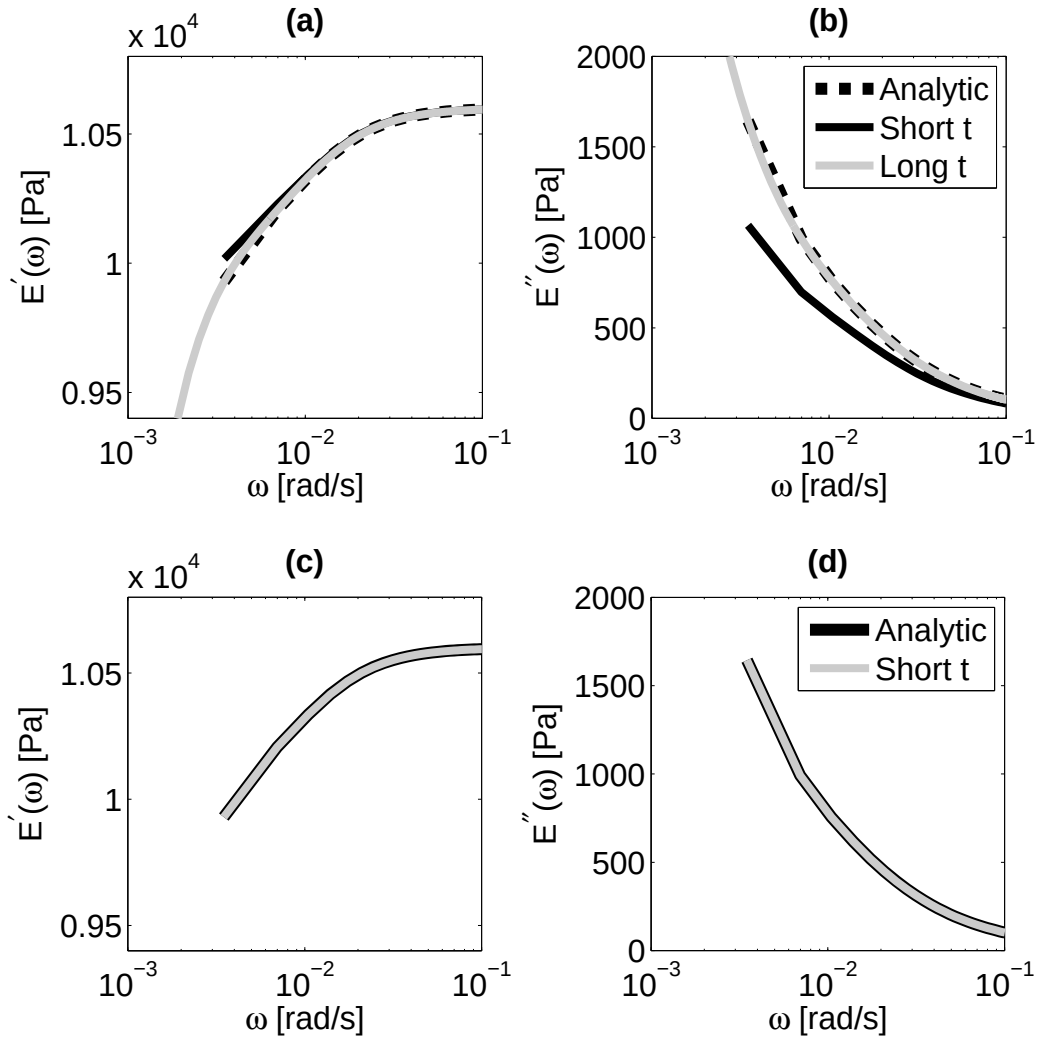

Figure 4.10: Figures **(a)** and **(b)** display $E^*(\omega)$ estimated from approach 1 processing of short and long time acquisitions of 'stress relaxation' data in comparison to the analytic solution. Figures **(c)** and **(d)** display $E^*(\omega)$ estimated from the short time acquisition of 'creep' data processed using approach 1 in comparison with the analytic solution.

component than the storage component.

4.1.4 Systematic Error

The values obtained for gelatin gels is highly dependent on experimental methods, gel construction, environmental conditions, ect. Thus there are no 'right' or 'wrong' values associated with gelatin gels in general. However, in this study gelatin gels are used to study polymer behavior and develop measurement methods. So it is necessary to produce a gel with consistent properties. We have observed that the thermal history of gelatin gels can be a major source of systematic error amongst gel sample sets. In this section we describe ways to ensure consistent results when comparing across sample sets by studying the measurement variabilities. Three different batches, all at the IEP, are considered. The first two each contain 4 samples that polymerized under similar average storage temperature $\bar{T}$ conditions over t_p. $\bar{T}$ was determined by averaging the storage temperature recorded at three equally spaced time intervals over t_p. The third batch contained 3 samples that polymerized at a higher $\bar{T}$.

Figure 4.13 displays how the average elastic modulus $\bar{E}_0$ varies with $\bar{T}$ for the 3 batches. The results of this study indicated that E_0 measurements for gelatin gels are sensitive to modest variations in storage temperature. When all 11 samples from the three batches are considered as drawn from a single distribution, the sample standard deviation is for $\bar{E}_0$ is 10%. If only the samples from the first two batches are considered, the sample standard deviation is 2%. These results indicate that it is important to maintain $< 1°C$ $\bar{T}$ differences between gel sample batches to avoid systematic error in E_0 measurements.

4.1.5 Instrumentation Error

The TA.XT texture analyzer was used for creep and stress relaxation measurements on gel samples. To assess the noise due to instrumentation, the mass ($m(t)$) output by the load cell under zero-load and zero-displacement conditions was recorded over 3600 s and sampled every 0.1 s. For direct comparison with creep and stress relaxation measurements, the mass data was converted to stress under the assumption of uniaxial compression in the direction normal to the load cell to calculate force ($F(t) = m(t)g$, where $g = 9.8$ m/s^2), and the cross-sectional area calculated using the diameter of gel samples (see section 3.2). This process was repeated 15 times and the Noise Power Spectrum (NPS) was computed for each experiment and averaged ($\text{NPS}_{avg}(\omega)$) over 15 experiments according to equation 4.9, where L is the number of data sets, N is the number of points per set, and $F_l(\omega)$

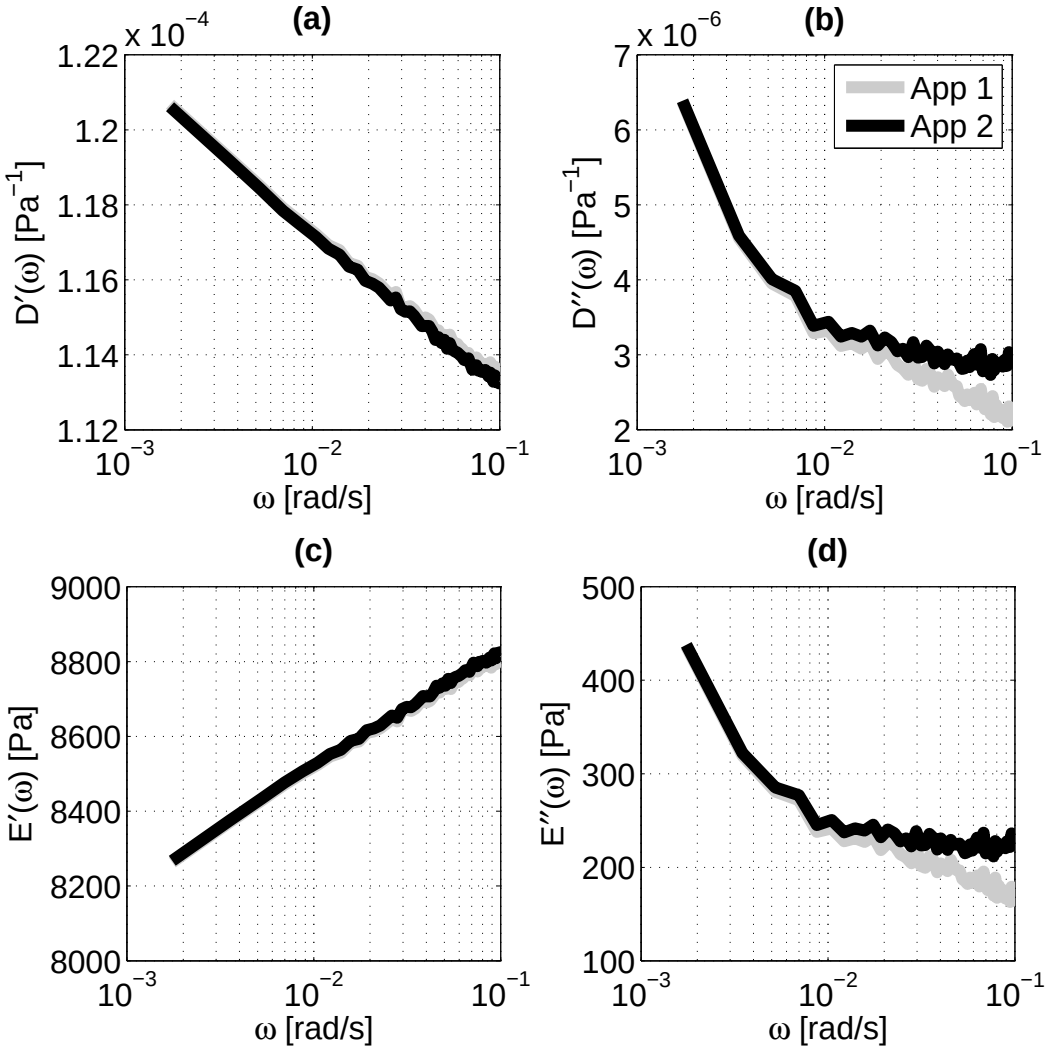

Figure 4.11: Figures **(a)**,**(b)** display the storage ($D'(\omega)$) and loss ($D''(\omega)$) compliance spectra for a representative creep measurement processed under approach 1 (App 1) and approach 2 (App 2). Figures **(c)**,**(d)** display the corresponding storage ($E'(\omega)$) and loss ($E''(\omega)$) modulus spectra.

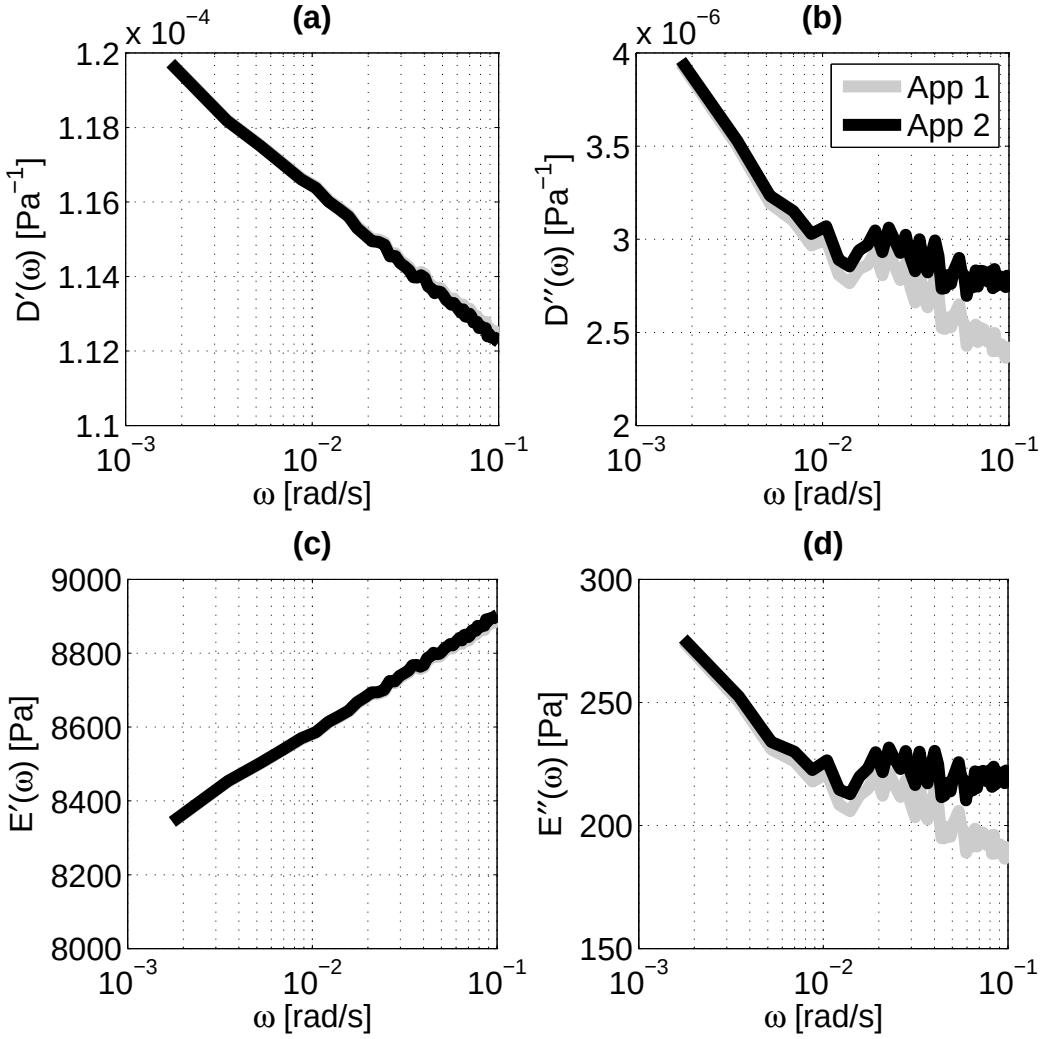

Figure 4.12: Figures **(a)**,**(b)** display the storage ($D'(\omega)$) and loss ($D''(\omega)$) compliance spectra for a representative stress relaxation measurement processed under approach 1 (App 1) and approach 2 (App 2). Figures **(c)**,**(d)** display the corresponding storage ($E'(\omega)$) and loss ($E''(\omega)$) modulus spectra.

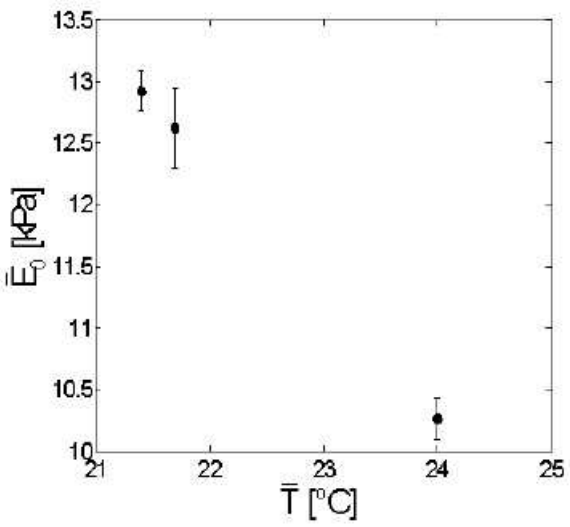

Figure 4.13: Variability in average elastic modulus $\bar{E}_0$ with average storage temperature $\bar{T}$. $\bar{E}_0$ values were determined from the 40th cycle of stress-strain preconditioning. The associated error bar is ± 1 sample standard deviation.

is the Fourier transform of set l. A sample time domain data set and the average NPS is displayed in figure 4.14.

$$\mathrm{NPS}_{avg}(\omega) = \frac{1}{L}\sum_{l=1}^{L}\frac{1}{N}|F_l(\omega)|^2 \tag{4.9}$$

It is evident from the time domain data that there is a slight drift in the stress measurements over time. This drift becomes evident in the NPS as the low frequency noise component. With the exception of this low frequency noise increase, white noise is evident across other frequencies.

In creep and stress relaxation measurements, the high frequency information occurs at short times and the low frequency information occurs at long times. Thus, the longer time measurements will be more affected by the low frequency noise due to instrumentation drift. But, in the case of creep measurements, the signal-to-noise ratio (SNR) will continue to increase over time because strain increases.

To reduce the effect of instrumentation noise in spectral analysis, I developed a noise reduction technique. For creep measurements, this technique requires estimating $D^*(\omega)$ for different lengths of time. To start, a short period of time is analyzed that will give the spectrum range for high frequencies, then a slightly longer time duration is analyzed. The spectrum from this second set extends to lower frequencies because the increased acquisition time increases the bandwidth of the

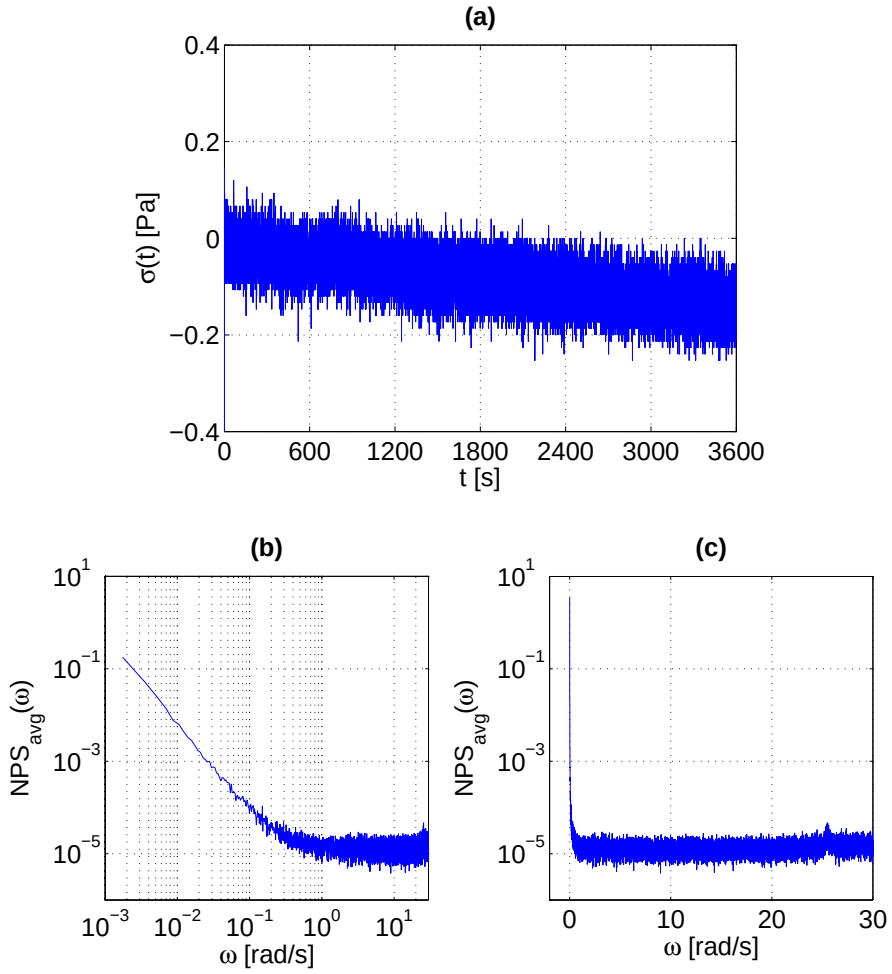

Figure 4.14: Figure **(a)** displays a representative plot of the noise of acquired $\sigma(t)$ data. Figure **(b)** displays the average noise power spectrum of 15 independent tests on a log-log scale. Figure **(c)** displays the same as **(b)** but with a linear ω scale.

frequency response. The low-noise portion of the second set is attached to the spectrum of the shorter time piece. This process is continued until the entire frequency range is accounted for. Only the low noise components for each length of time are utilized. This processing works because for each frequency, all the time domain data will effect the result due to taking a Fourier transform. Thus, less accumulated noise will result for shorter lengths of time. An example of this technique for the $D^*(\omega)$ estimate obtained from a creep experiment processed according to approach 1 case **a** is displayed in figure 4.15.

4.2 Elasticity Imaging

Elasticity imaging was performed on three phantoms injected with fluid at three different pH levels as described in section 3.3. As shown in figure 4.16a, the standard ultrasonic B-mode image shows little to no contrast near the injection site. The procedure for imaging viscoelastic parameters is provided elsewhere [35]. We obtained ε_0 images for all three phantoms, and a β image for the acid injection phantom as displayed in figure 4.16b,d,f (ε_0 image for the control pH 5.6 phantom is not displayed). To evaluate elasticity pH imaging, an understanding of the mechanical properties of the gel under differing pH conditions is necessary, and the true pH of the inclusion must be known. To accomplish these tasks, the following two approaches have been taken:

1. Use ε_0 and β images from gel phantoms to obtain E_{CR} and β_{CR}^{-1} parameters for comparison with creep and stress relaxation measurements.

2. Use the images of the pH indicator gels to predict the pH distribution in the gel phantoms.

To implement the first approach, a point-by-point inverse of the ε_0 and β images was taken to represent images approximately proportional to E_0 and β^{-1} images. The relationship is approximate because in practice the stress distribution is not spatially uniform. However, for the low strain contrast in this study, the inverse technique under the assumption of a uniform stress is a good approximation [27]. It is assumed that the pH of the background of the gel phantom is 5.6 when estimating E_{CR} and β_{CR}^{-1}. Lateral profiles of each image were taken from the average of the axial data in the outlined regions displayed in figure 4.16. Profiles are displayed in figure 4.16c,e,g.

The acidic phantom ε_0 image (figure 4.16b) shows local softening (bright strain), which corresponds to a reduced modulus as emphasized by the E_{CR} profile (figure 4.16c). This phantoms β image (figure 4.16d) also shows a brightening about the injection site. The corresponding β_{CR}^{-1} profile (figure 4.16e) gives a minimum near 0.7. By comparing the E_{CR} and β_{CR}^{-1} profiles from the acidic

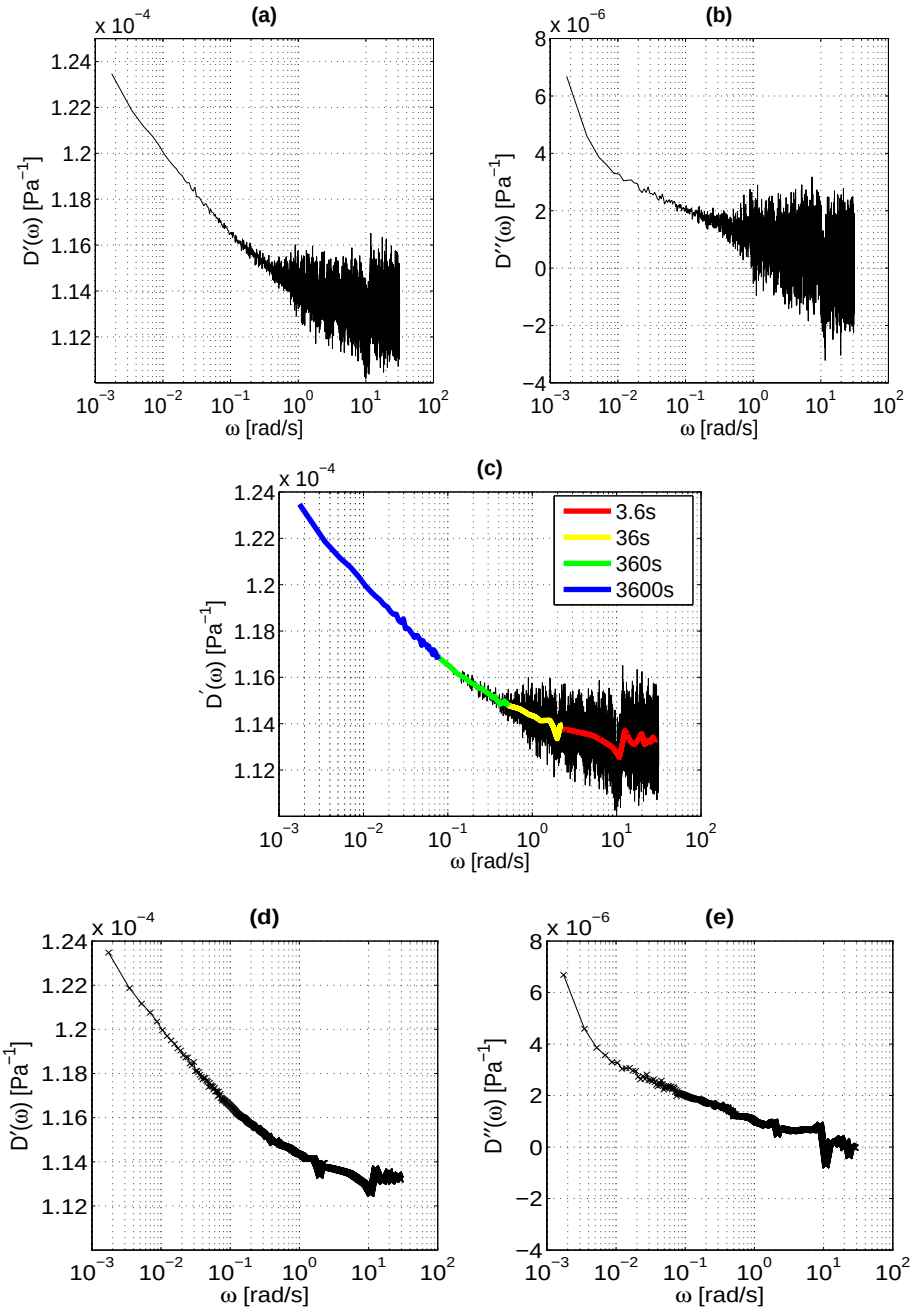

Figure 4.15: Figures **(a)** and **(b)** display the storage ($D'(\omega)$) and loss ($D''(\omega)$) compliance respectively from a representative creep measurement processed according to case **a** approach 1. Figure **(c)** displays the original $D'(\omega)$ spectra for all 3600 s of data, as well as $D'(\omega)$ obtained from the low noise portion of shorter time segments of $D(t)$ data. The times are listed in the legend. Figures **(d)** and **(e)** display the low noise spectral estimates of $D'(\omega)$ and $D''(\omega)$ respectively; these estimates were obtained by using the time segments listed in figure (c).

phantom images to the E_{CR} and β_{CR}^{-1} values obtained from gel samples at pH 4.6 (figure 4.3a,b), we infer that the center pH of the acid phantom is approximately 4.6. The pH increases outward from the center of the injection until it reaches pH 5.6 resulting in a spatial distribution of pH covering approximately 1.5 cm.

The ε_0 image of the control pH 5.6 phantom (not displayed) and the corresponding E_{CR} profile (figure 4.16c) shows some softening near the injection site, suggesting a structural weakening of the polymer as a result of excess fluid and tube withdrawal during polymerization.

The base injection phantom ε_0 image (figure 4.16f) and E_{CR} profile (figure 4.16g) indicate that the center of the phantom is soft with an E_{CR} close to the background, but moving outwards from the center a stiffening effect is observed. The E_{CR} values associated with the two peaks surrounding the center in figure 4.16g are approximately twice the maximum E_{CR} measured with the creep and stress relaxation experiments in figure 4.3a. The size of the base inclusion is larger than that of the acid inclusion with a diameter of approximately 2.5cm. The differences in size of the inclusions and the high E_{CR} values observed in the base phantom may be the result of the gels enhanced buffering capacity to acids in comparison to bases. It was seen in table 3.1 that a much greater volume of acid was required to shift the pH of the gels to a lower value than the amount of base needed to shift the pH upward.

The second approach to the evaluation of pH induced elasticity imaging is to estimate the pH distribution of the pH injection phantoms using color contrast from gels with indicator solution. To calibrate for the colors associated with different pH levels, individual gel samples were created with the pH indicator solution at the same three pH levels 4.6, 5.6, and 6.6 used for creep and stress relaxation measurements (figure 4.17). Gray scale images provided the best contrast between pH 4.6 and pH 5.6 gels (figure 4.18a,b), and analysis of the red colors present in the RGB color space provided the best contrast between pH 6.6 and pH 5.6 (figure 4.18c,d). This analysis was first performed on the homogenous pH indicator gel samples in order to find contrast standards for this study and then applied to the phantoms. Regions of each gel sample image were analyzed by finding the mean and standard deviation of the color intensity. Then contrast ratios of the mean values with respect to pH 5.6 were taken. To be consistent with E_{CR} and β_{CR}^{-1} measurements, the contrast ratios were normalized by the pH 5.6 gel values and therefore the more acidic gels measured less than one and the more basic gels measured greater than one. The contrast ratios are presented in figure 4.19a.

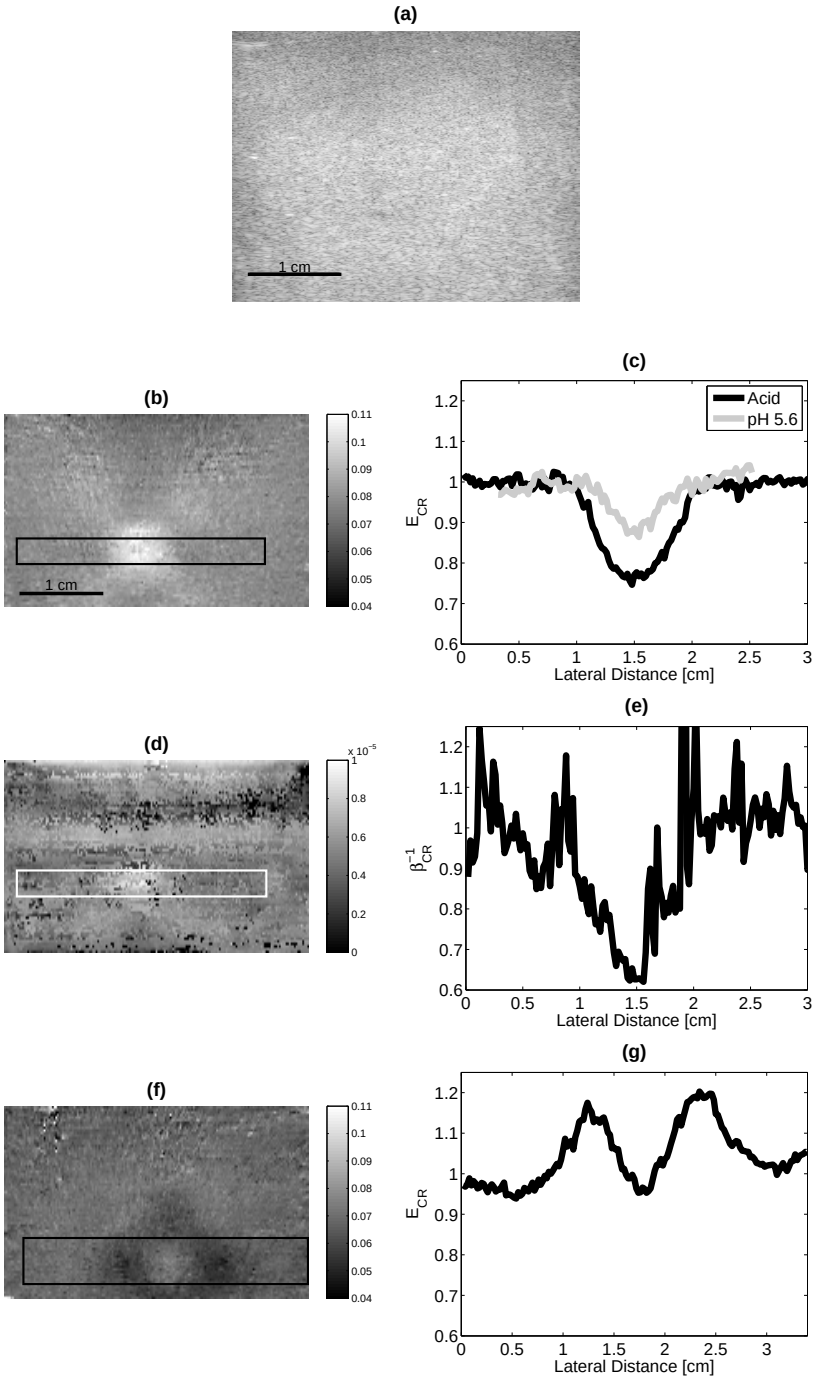

Figure 4.16: **(a)** is a representative ultrasonic B-mode image of an injection phantom. **(b)** is the ε_0 image of the acid injection phantom and **(c)** displays the corresponding E_{CR} profile relative to the background along with the E_{CR} profile for the control pH 5.6 injection (ε_0 image not shown). **(d)** is the β image of the acid injection phantom and **(e)** displays the corresponding β_{CR}^{-1} profile. **(f)** is the ε_0 image of the base injection phantom and **(g)** displays the corresponding E_{CR} profile. Rectangular regions in the images show the areas from which the profile plots to the right were obtained.

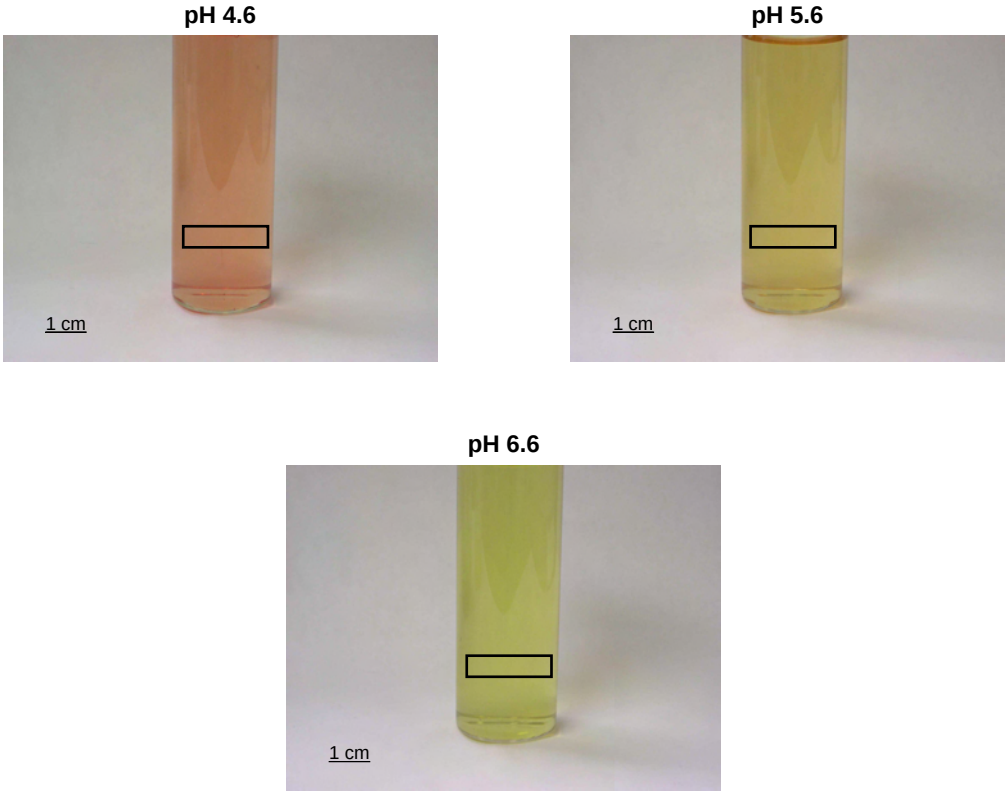

Figure 4.17: This figure includes the original pictures taken of gels of known pH with the pH indicator solution added. The pH indicator solution causes the gel color to change based upon the pH of the gel. Images are of gels of pH 4.6, 5.6, and 6.6 as indicated.

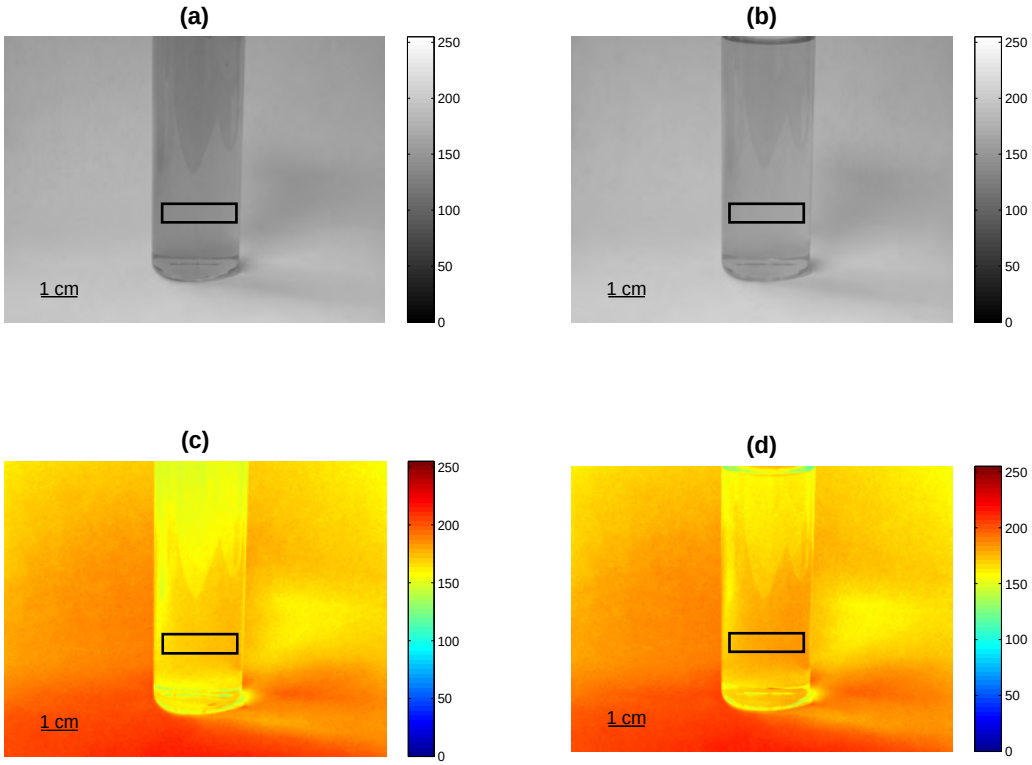

Figure 4.18: This figure includes the contrast images used to find contrast between different pH levels based upon color differences when the pH indicator solution was used. **(a)** and **(b)** are gray scale images of gels with pH 4.6 and 5.6 respectively. **(c)** and **(d)** are images of just the red component of the images of gels pH 6.6 and 5.6 respectively. Gray scale is used to detect pH contrast for pH $<$ IEP gels and red images are used to detect contrast for pH $>$ IEP gels.

Applying this same analysis technique to the injection gel phantoms with pH indicator solution (photographs displayed in figure 4.19b,c) requires the assumption that the background of the gel is pH 5.6. In a similar manner to the ε_0 image processing, lateral contrast ratio profiles from the selected region depicted on the gray scale and red images (figure 4.19d,e) were analyzed. The profiles, as seen in figure 4.19f,g, in comparison to the contrast ratios presented in figure 4.19a, suggest that the peak pH due to the acid injection is slightly lower than 4.6 and the width of this peak is approximately 2 cm. The basic injection gel phantom has a centrally located maximum pH with contrast approximately four times that found for the pH 6.6 color contrast. The width of this peak is approximately 2.5 cm, which is in agreement with the width determined from the elasticity imaging study. The spatial distribution of pH in the heterogenous gel phantoms is a result of a high concentration of acid or base diffusing outward from the center of the injection site. Initially, the acid and base is very concentrated at the center. At the time of injection the gelatin solution has not completely polymerized, thus the acid or base freely diffuses outward.

Because the basic injection gel phantom has contrast outside the range of the known pH contrast, it is likely that the pH at the center of the phantom is much greater than 6.6. The pH indicator gel profile (figure 4.19g) does not have a contrast minima located in the center of the inclusion as it does for the E_{CR} profile in figure 4.16g. This observation suggests that gels become softer when a critical pH level is exceeded; this type of behavior was previously observed by Cumper and Alexander for Type B gelatin gels with a similar IEP [6]. Rigidity (shear modulus) data reported by these authors has been reproduced in a modified version to represent E_{CR} contrast as seen in figure 4.20. In terms of E_0, it is reasonable to assume that contrast evident from the the shear modulus (G) is the same as that for the initial elastic response of unconfined uniaxial compression under the assumption of an incompressible material such that $E_0 = 3G$ [37]. Analysis of the data presented in Cumper's study suggests that G is maximum at approximately pH 10. The E_{CR} for pH 10 is about 1.2, which is the approximate maximum E_{CR} evident from the basic injection phantom (figure 4.16g). According to Cumper, the E_{CR} near pH 11 is similar to that of pH 5.6, thus it is reasonable to assume that the center of the basic injection phantom has a pH near 11.

In both the acidic and basic injection phantoms, it is likely that the structural defect observed in the control pH 5.6 phantom (see figure 4.16c) caused by the injection, contributes to some of the central softening observed in the ε_0 images. However, this effect is smaller than the softening due to an acid injection as illustrated by the comparison of E_{CR} profiles in figure 4.16c and is unlikely the dominant source of strain contrast.

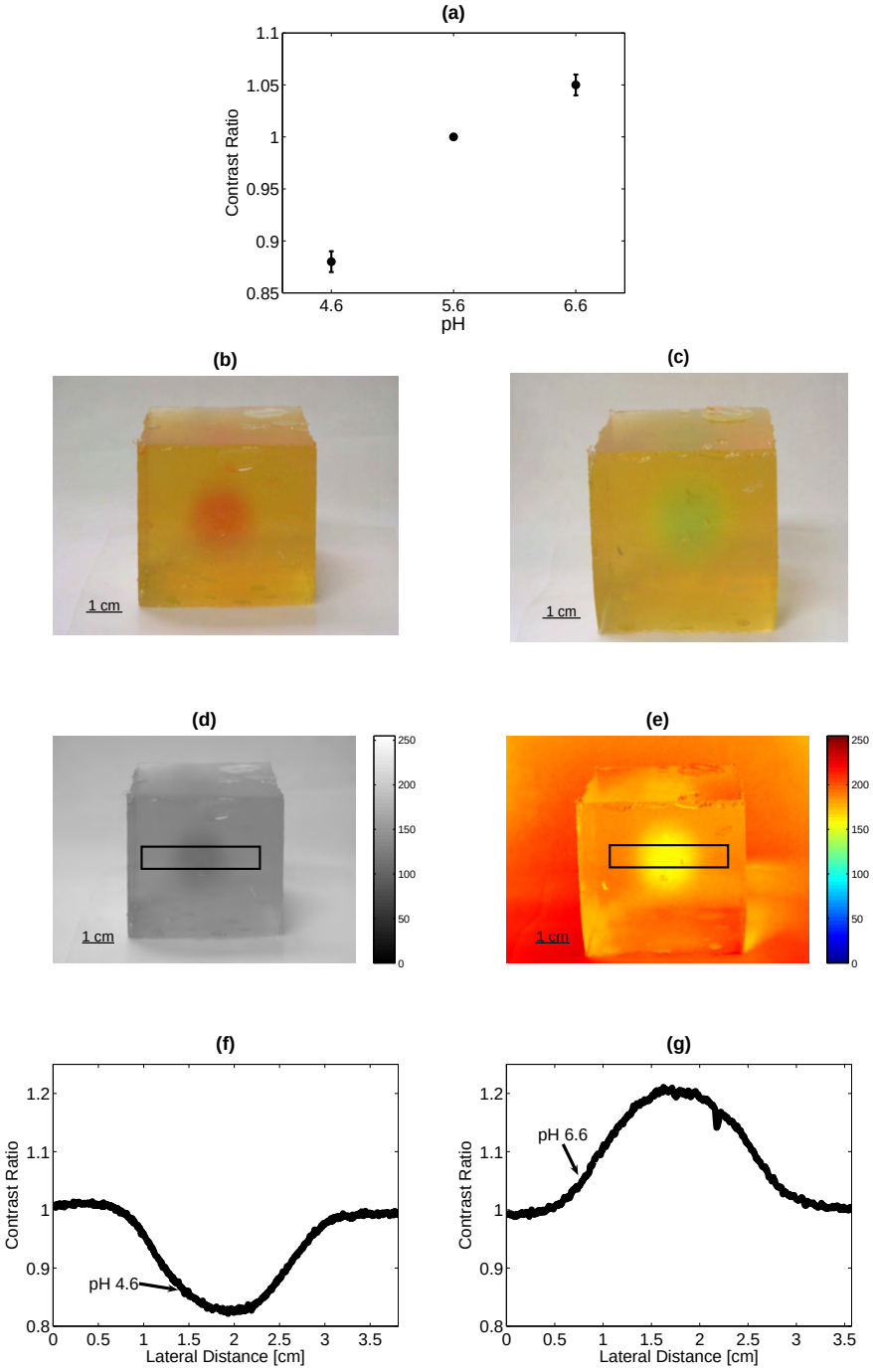

Figure 4.19: **(a)** displays the contrast ratios for individual pH values based upon the pH indicator solution contrast in gel samples. **(b)** and **(c)** display the photographs of the acid and base injection phantoms respectively. **(d)** displays the gray scale image of the acid injection phantom with pH indicator solution and **(f)** is the corresponding contrast ratio profile. **(e)** displays the red image of the base injection phantom with pH indicator solution and **(g)** is the corresponding contrast ratio profile.

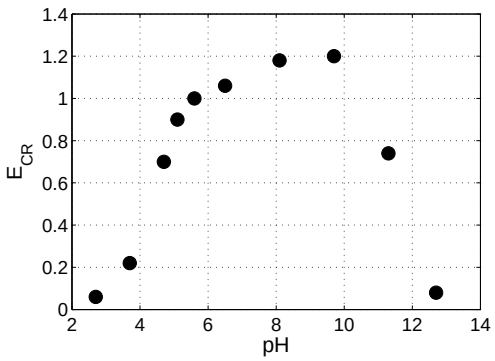

Figure 4.20: Approximate E_{CR} values vs pH from the original data of Cumper and Alexander [6]. The data presented in this figure is a modified version of that originally published by AJSR. The data value at pH 5.6 was not provided by Cumper and Alexander we interpolated this value from the 2 data points surrounding pH 5.6. Permission to reproduce this modified version of the data was granted by **CSIRO** Publishing. The full text of Cumper and Alexander's article can be accessed via either subscription or pay-per-view services at http://www.publish/csiro.au/nid/52/issue/3400.htm.

In addition to the analysis of pH contrast at $t_p = 48$ hours, the spatial change in pH after $t_p = 9$ days was also analyzed. The E_{CR} determined from E_0 measurements on homogeneous gel samples tested with creep and stress relaxation indicates that pH contrast remains approximately constant ± 1 pH unit about the IEP with respect to the $t_p = 48$ hour measurements (see figure 4.3a). However, with increased t_p, the gels get stiffer as indicated by the E_0 measurements reported in table 4.2.

On the other hand, the heterogeneous acid and base injection phantoms possess a pH gradient and we found that the pH distribution for these phantoms does not remain constant with time. Low noise photographs of the pH indicator phantoms were not obtained at $t_p = 9$ days, however, cross-sectional photographs of the pH indicator phantoms at $t_p = 48$ hours and $t_p = 9$ days are displayed in figure 4.21. In both cases, the acid and base injection causes a more concentrated pH change at the center after $t_p = 48$ hours than for $t_p = 9$ days. After 9 days, the acid and base appear to have diffused further outward and are not as concentrated at the center.

Comparison of the ε_0 images generated from elasticity imaging measurements at $t_p = 48$ hours and $t_p = 9$ days indicates that the E_{CR} contrast from the pH 5.6 (control) injection phantom is not significantly affected over t_p in the range of 2-9 days (see figure 4.22b). However, the E_{CR} of the acid and base injection phantoms are affected over this t_p range (see figure 4.22a,c).

The central minimum of the acid injection phantom for $t_p = 9$ days is higher than that at $t_p = 48$ hours (figure 4.22a). In comparison with the pH distribution change illustrated in figure 4.21a,b, this indicates that over time as the acid diffuses away from the center, the structural weakening is

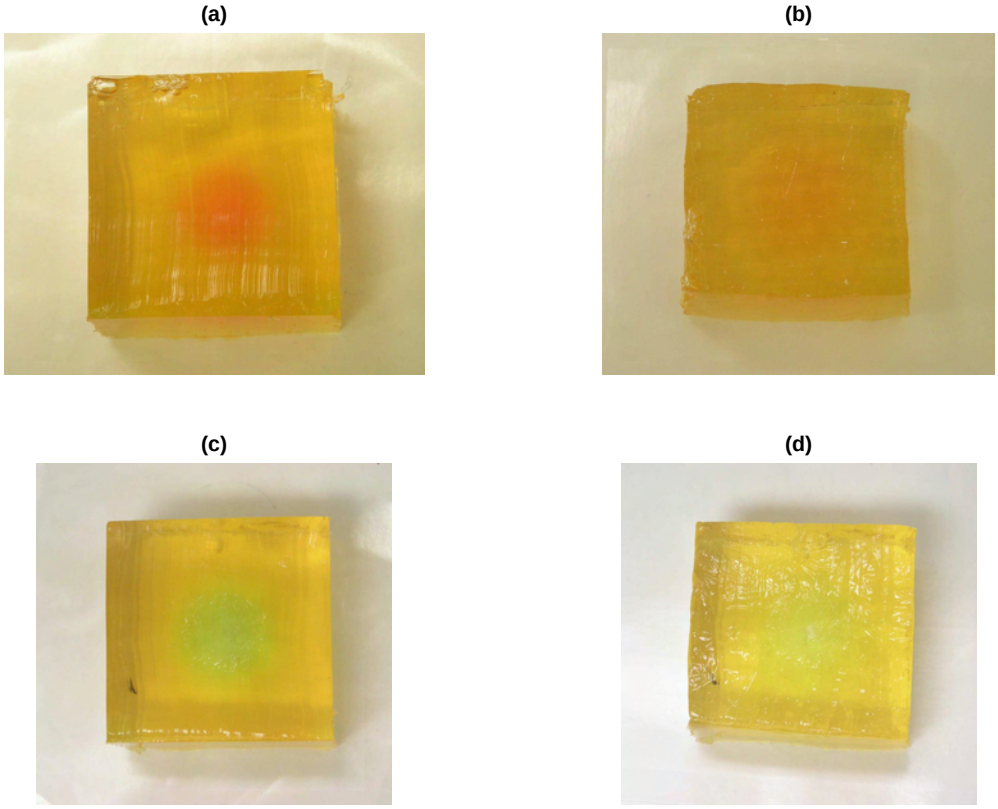

Figure 4.21: **(a)** displays the photograph of the acid injection pH indicator phantom after $t_p = 48$ hours. **(b)** displays the photograph of the acid injection pH indicator phantom after $t_p = 9$ days. **(c)** displays the photograph of the base injection pH indicator phantom after $t_p = 48$ hours. **(d)** displays the photograph of the base injection pH indicator phantom after $t_p = 9$ days.

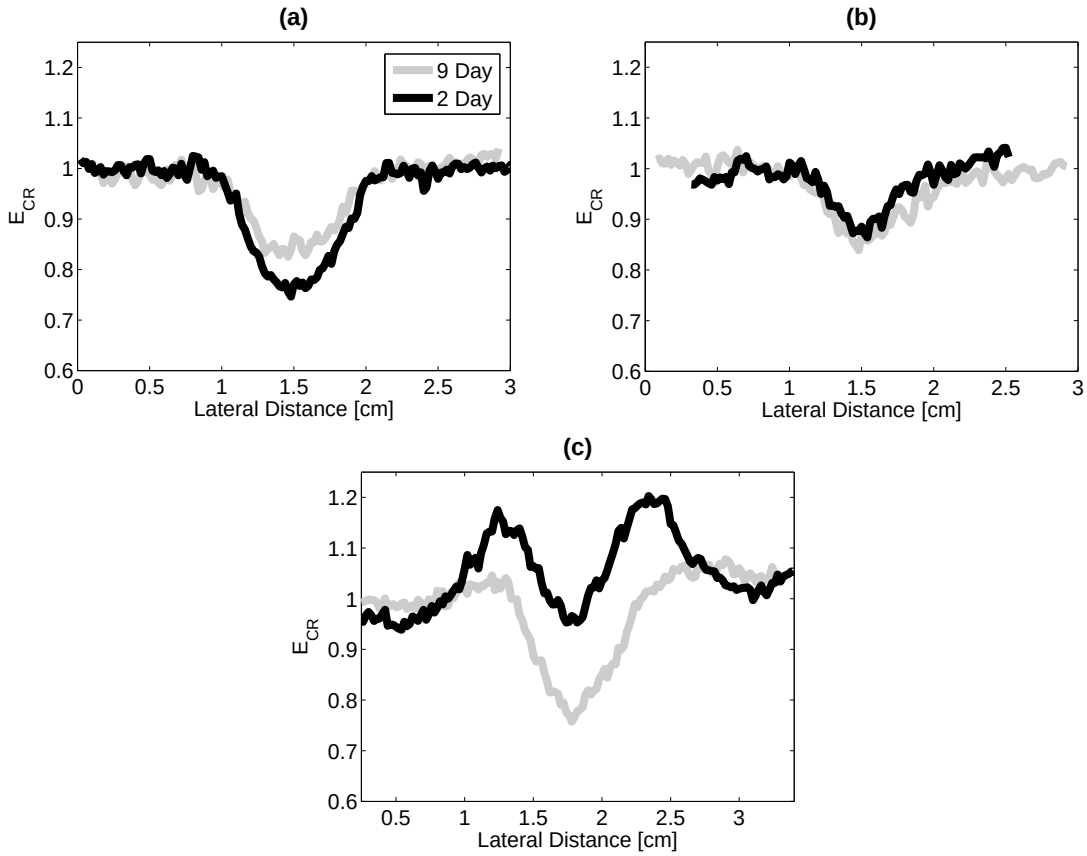

Figure 4.22: **(a)** displays the E_{CR} profile of the acid injection phantom for $t_p = 48$ hours (2 days) and $t_p = 9$ days. **(b)** and **(c)** display the similar profiles for the pH 5.6 (control) injection phantom and the base injection phantom respectively.

not as enhanced at the center because a lower concentration of acid is present locally.

The E_{CR} profile of the base injection phantom also changes with t_p. In a similar manner to the acid injection phantom and based upon the pH indicator results, we believe that as the base diffuses outward from the center, the local concentration is reduced, yet locations outward from the center will have higher local concentrations of base. Based upon the results of Cumper et al. [6], we expect to see a higher E_{CR} value at the center of the phantom for $t_p = 9$ days than for $t_p = 48$ hours. We would also expect that the location of the local maxima would move further away from the center and the E_{CR} at their original locations would decrease. However, inspection of the 9 day E_{CR} profile (figure 4.22c) does not verify either expectation. We believe there are two possible explanations for this discrepancy:

1. The field-of-view (FOV) is not sufficient to capture the full E_{CR} distribution of pH.

2. The presence of a soft region confined in a stiffer background reduces the contrast-transfer efficiency for the $t_p = 48$ hour E_{CR} profile.

For explanation 1, if the elastic modulus distribution is assumed to take the form of that observed for $t_p = 48$ hours, the general shape would look like that shown in figure 4.23a, where it is assumed that region 1 is pH=5.6, region 2 is 5.6<pH<10, and region 3 is pH>10. If the FOV in the ε_0 image is large enough to capture all regions, then the proper E_{CR} ratios with respect to pH 5.6 can be obtained for all three regions. However, if the FOV is not sufficiently large, errors may arise in E_{CR} estimates. For instance, consider the situation where the profile displayed in figure 4.23b is the only data available in the FOV. If this data is processed under the assumption that region 2 = region 1, an improper E_{CR} profile would be obtained and would take the form of that observed for $t_p = 9$ days.

Explanation 2 is based upon the work by Ponnekanti et al. [27]. In their study, the contrast-transfer efficiency (the ratio of the elastic contrast measured from the ε_0 image to the true contrast) is evaluated for various conditions of elastic inhomogeneity. They found that soft regions confined in stiff backgrounds had a continuously decreasing contrast-transfer efficiency with increasing true contrast. This reduction in efficiency causes soft regions to appear stiffer than they really are. With respect to the E_{CR} profile of the base injection phantom, the $t_p = 48$ hour phantom possesses a central soft region surrounded by a stiff region. Because of the response of type B gelatin gels to base (see figure 4.20), the contrast between the local maxima and minima is likely quite large; indicating that the true contrast between these regions is high. It is possible that the E_{CR} of the central peak

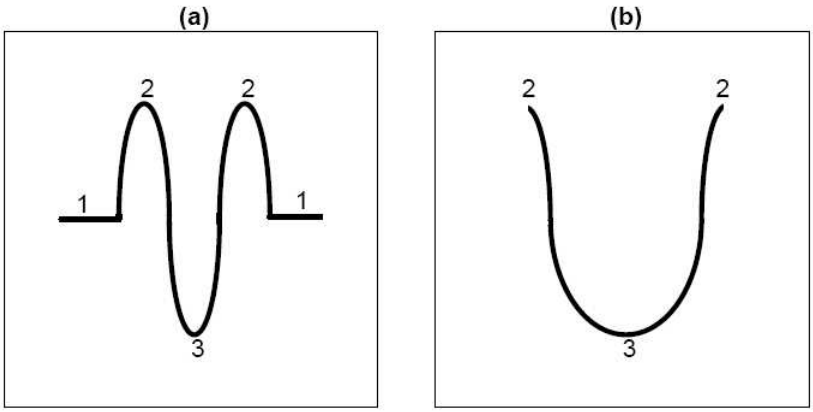

Figure 4.23: Figure **(a)** displays a possible elastic modulus contrast profile pattern for the $t_p = 48$ hour base injection phantom. Figure **(b)** displays the same for the $t_p = 9$ day phantom. Regions described in text are labeled numerically.

is over estimated due to a reduced contrast-transfer efficiency. We know after $t_p = 9$ days the base has diffused outwards from the center, thus causing a lower local concentration of base at the center. However, further from the center, the base concentration has likely increased. The local maxima peaks are likely reduced due to the addition of base as predicted by the E_{CR} ratios predicted by Cumper et al. [6] in figure 4.20. Since there is no longer an apparent stiff region surrounding a soft region, the contrast-transfer efficiency is improved for $t_p = 9$ days, therefore we can expect a better estimate of the elastic contrast in the soft region.

These results suggest that over time a pH gradient will cause a continuous diffusion of acid and base. This variation in pH will alter the elastic properties of the gel and can be monitored by analysis of E_{CR} profile changes. Since the E_{CR} contrast with pH ± 1 unit about the IEP at $t_p = 48$ hours is approximately equal to that at $t_p = 9$ days (see figure 4.3a) the pH distribution by E_{CR} values may be compared over varying polymerization times.

Recall that base injection phantoms were constructed and analyzed for completeness of the pH study; basic conditions are not a expected clinically. Thus, the major complications associated with interpreting elasticity images of pH contrast (primarily present for pH>IEP) is likely not a concern for clinical applications.

Chapter 5

Discussion

Figures 4.1 and 4.5 show that the amplitudes of the VE Voigt units representing creep data are similarly affected by pH: in all cases strain decreases with pH as the gel stiffens. We also found that the VE time constants in figure 4.1 are insensitive to pH changes. Consequently, the principle VE effects of pH on the hydrogel within ± 1 pH unit of the IEP appear to be elastic and not viscous.

Furthermore, in a study where finite-element model results were fit to gelatin hydrogel creep measurements for the unconfined geometry typical of elasticity imaging, we found that fluid motion in the gel occurs quickly (seconds) and is a relatively small component of the observed creep response [21]. This observation suggests that time-varying strain in hydrogels at any pH near the IEP is dominated by elastic and viscoelastic responses of the collagen matrix more than the poroelastic response from fluid flowing through the matrix. Therefore we should study how the collagen matrix changes with pH to understand the corresponding creep responses.

Individual fibers of type I collagen, as found in gelatin and breast stroma, deform elastically [3]. However, the connections among fibers that determine hydrogel dynamics are primarily weak molecular bonds. These bonds regulate gel stiffness depending on the net electric charge density of the collagen molecules, and pH will affect the charge density.

The triple-helix structure of native collagen is stabilized internally by inter-chain hydrogen bonds and is efficient at cross linking with other helices [1, 16]. Denatured forms of collagen, e.g. gelatin, have a lesser proportion of triple helices due to partial renaturation in the gel state [7], and therefore gelatin gels are more fragile than native forms at the same collagen concentrations. Increasing pH above the IEP during gelation favors the formation of helical structures in gelatin gels [23] that results in the greater storage modulus [20] of the gel we observed at higher pH values. Decreasing the pH below the IEP has the opposite effect. In addition, IEP gels have the largest average molecular weight. Increasing or decreasing the pH from the IEP degrades the gelatin molecules, although the amount of degradation is greater for acidic gels [23], resulting in shorter gelatin fragments. Also, the net positive charge for pH<IEP gels is much lower than the net negative charge for pH>IEP gels

for equal deviations from IEP. The excess charge is likely to elongate the polymer chain [23]. pH adjustments also induce structural changes in collagen [29, 30, 38]. Roeder et al. [29] found that an increase in pH produced fibrils of longer length, while a decrease in pH resulted in shorter collagen fibrils. The same study found that the elastic modulus increased with pH as a consequence of fibril length. Longer fibrils increase the mechanical integrity of the collagen network.

Similar modulus measurement trends were observed by Seehra and Silver [30] when studying tissues subjected to pH changes. They attributed the enhanced modulus at basic pH to the high excess of net negative charges on a collagen molecule indicating that repulsive forces between molecules may prevent flexible regions from deforming resulting in strain hardening. This combination of the change in average molecular weight, fraction of helical structures, charge density, and polymer length with pH favors a predominantly elastic response to pH variations that we (figure 4.3) and others (figure 4.20) have observed in hydrogels and connective tissue.

Our hypothesis is that the pH effects on VE properties observed in hydrogels can serve as a model for pH effects on breast stroma elasticity. As a focal grouping of cancer cells rapidly grow beyond the capacity of the local blood supply, the extracellular pH in that region is reduced. Consequently, as tropocollagen segments emerge from stromal fibroblast cells, the acid conditions reduce their ability to self assemble into long ECM fibers. We simulated the conditions of acidic breast stroma through changes in pH during gelatin polymerization. It is important to change the pH at the appropriate time in gel formation. We originally attempted to inject acids and bases into cross-linked gels, but quickly found that osmotic forces drew fluids to the injection site depending on the ionic concentration. Regardless of the pH we always found that the injection site was much stiffer than the surrounding gel. Changing pH during gelation gave an imaging response consistent with that of the uniform gel samples and the pH indicator gels.

At pH values in the range of $\pm$ 1 unit about the IEP, the elastic modulus of hydrogels increases with pH. For gelatin gels IEP = 5.6 and for collagen IEP $\simeq$ 7 [18, 38]. The observed pH effects on mechanical properties are predominantly elastic, which is consistent with the literature describing how pH can influence the molecular structure of collagen. Although we did not specifically investigate the spatial resolution of elasticity imaging methods for detecting pH changes, the imaging results shown here suggest that the spatial resolution of pH-induced contrast is comparable to other important types of strain image contrast, such as variations in collagen density [22]. Insofar as gelatin hydrogel measurements mimic breast stroma, it seems that acidic breast tumors may be more detectable through contrast in elastic strain images than viscoelastic (time-varying strain)

image properties, at least in the quasi-static bandwidth of force stimuli. We found recently that nonpalpable breast lesions can be classified as malignant or benign based on contrast in the time constant T_1, and that elastic strain was not discriminating between these classes [28]. Therefore we conclude that extracellular pH is not likely to be a diagnostic indicator for malignant-benign discrimination. Acidic tumors are more dangerous clinically and will have lower elastic strain contrast than equivalent tumors of normal pH.

In this study, a macro-scale interpretation of how pH effects tissue mimicking phantoms mechanically was developed. Insight into the components responsible for pH induced mechanical contrast is limited to interpretation of elastic, viscoelastic, and viscous components of the network based upon time domain curve fitting of data as well as $E^*(\omega)$ analysis. The gel network can be envisaged as having an elastic response from the protein network, a viscoelastic response from a coupled response between the protein network and structured fluid, and a viscous response from loosely bound fluid. A micro-scale understanding of pH effects can potentially be achieved using Fourier Transform Infrared Spectroscopy (FTIR). FTIR spectroscopy provides information about protein structure. Secondary and quaternary protein structural information is obtainable for collagen and gelatin networks. Work is underway for monitoring the mechanical response of gelatin hydrogels under compression with FTIR. If successful, FTIR should provide valuable information regarding the role of hydrogen bonding, structural water, and higher order structures to VE effects observed macroscopically. Successful macro- and micro-scale techniques and interpretation of pH induced contrast in the simple gelatin hydrogel model pave the way for applying these methods to more advanced tissue models and stromal tissue.

Appendix A

A.1 Processing Procedures for Estimating $D^*(\omega)$ and $E^*(\omega)$

The following sections describe the procedures used for estimating $D^*(\omega)$ and $E^*(\omega)$ for creep and stress relaxation measurements. These procedures were developed based upon the assumption that the Voigt and Maxwell models presented in section 2.2.1 are representative of the experimental data analyzed. Generalized versions of the models are assumed. All procedures describe processing using Matlab (Mathworks Inc.).

A.1.1 Creep: Approach 1

For case **a**, the first step is to take a time derivative of the $D(t)$ data. This is accomplished by using the Matlab function '`diff`', which calculates the difference between adjacent data points. This method is a good approximation if the sampling rate is high enough. I have found that a rate of 10 samples/sec is sufficient for processing these experiments. A generalized version of equation 2.12 in terms of compliance rather than strain is:

$$D(t) = \frac{\varepsilon(t)}{\sigma_a} = D_0 + \sum_{k=1}^{K} D_k \left(1 - \exp\left(-\frac{t}{T_k}\right)\right) + \frac{\beta}{\sigma_a} t \qquad \text{, for } t > 0 \tag{A.1}$$

where β represents the $K+1$ long time VE element $\varepsilon_{K+1}/T_{K+1}$. The derivative of equation A.1 is:

$$\dot{D}(t) = D_0 \delta(t) + \sum_{k=1}^{K} \frac{D_k}{T_k} \exp\left(-\frac{t}{T_k}\right) u(t) + \frac{\beta}{\sigma_a} u(t) \tag{A.2}$$

where $\dot{D}(t)$ is the time derivative of $D(t)$ and $\delta(t)$ is the Dirac delta function. When using Matlab's '`diff`' function on data of this form, the elastic term $D_0\delta(t)$ does not get successfully incorporated into the result because of Matlab's inability to recognize the step function $D_0 u(t)$. Therefore to obtain the correct derivative of $D(t)$, this term must be manually inserted into the result. Fortunately,

this correction is trivial under approach 1 since it is just the value of $D(t)|_{t=0}$. The second step to finding $D^*(\omega)$ is to take the Fourier transform of $\dot{D}(t)$. This is accomplished by utilizing Matlab's '`fft`' function which outputs an N point DFT (discrete Fourier transform) where we choose N to be the length of the input data vector. The Fourier transform of equation A.2 is:

$$D^*(\omega) = D_0 + \sum_{k=1}^{K} \frac{D_k}{1 + i\omega T_k} + \frac{\beta}{i\omega\sigma_a} \tag{A.3}$$

There are also errors that need to be accounted for when taking the DFT of a this type of signal. The first problem is, Matlab's '`fft`' function is unable to recognize a unit step function. Thus, the term from the linear component needs to be corrected for. The other issue involves taking the '`fft`' of a delta function. Like, $u(t)$, $\delta(t)$ is also an injective function and needs to be corrected for. A way to approach this problem and avoid the above two issues, is to remove D_0 from the original time domain data and add it back into the frequency domain by way of the superposition principle. Doing this also eliminates the error generated when taking a derivative. Since the linear component can also be estimated and subtracted in the time domain, it is advisable to also remove this component and add it back to the frequency domain result by way of the superposition principle. Thus the following steps should be taken to obtain $E^*(\omega)$ for case **a**:

1. Estimate the linear term $\frac{\beta}{\sigma_a}t$ from $D(t)$
2. Subtract D_0 and $\frac{\beta}{\sigma_a}t$ from D(t) to get $D_{VE}(t) = D(t) - D_0 - \frac{\beta}{\sigma_a}t$
3. Take the derivative of $D_{VE}(t)$ to get $\dot{D}_{VE}(t) = \frac{d}{dt}D_{VE}(t)$
4. Take the '`fft`' of $\dot{D}_{VE}(t)$ to get $D^*_{VE}(\omega) = \mathscr{F}\{\dot{D}_{VE}(t)\}$
5. Add D_0 and $\frac{\beta}{i\omega\sigma_a}$ to $D^*_{VE}(\omega)$ to get $D^*(\omega) = D^*_{VE}(\omega) + D_0 + \frac{\beta}{i\omega\sigma_a}$
6. Invert $D^*(\omega)$ to obtain $E^*(\omega)$: $E^*(\omega) = \frac{1}{D^*(\omega)}$

For case **b**, a similar approach to that used in case **a** is taken. To process this case, steps 1-4, and 6 from case **a** should be followed. Step 5 needs to be modified to:

5. Add D_0 to $D^*_{VE}(\omega)$ to get $D^*(\omega) = D^*_{VE}(\omega) + D_0$

Case **c** is simpler than the previous two cases and only requires steps 1-4, and 6 from case **a** because we are only interested in the complex modulus of the viscoelastic response.

A.1.2 Stress Relaxation: Approach 1

The first step in calculating $E^*(\omega)$ is to take a derivative of $E(t)$ to obtain $\dot{E}(t)$. Like the creep data, the Matlab function, '`diff`', is used for calculating an approximate derivative. In theory $\dot{E}(t)$ for equation 2.15 should be:

$$\dot{E}(t) = \sum_{l=1}^{L} E_l \delta(t) - \sum_{l=1}^{L} \frac{E_l}{\tau_l} \exp\left(-\frac{t}{\tau_l}\right) u(t) \tag{A.4}$$

When using '`diff`' to attempt to achieve a result that follows equation A.4, the initial elastic response $E(t)|_{t=0} = E_0$ must be corrected for. However, if the end goal of taking the derivative of $E(t)$ is to eventually find $E^*(\omega)$, then the E_0 term does not need to be corrected at this step because of the superposition principle. It is beneficial to wait and add the E_0 term after taking the Fourier transform because the Fourier transform of a delta function is just a constant. Unlike the creep experimental data, it is not entirely possible to find a point in the stress-relaxation data after which the data remains constant because it is not possible to extract a purely linear term from this type of data. Thus the behavior at long times cannot be well modeled and superimposed into the frequency domain. In theory, the Fourier transform of equation A.4 is:

$$E^*(\omega) = \sum_{l=1}^{L} \frac{i\omega E_l \tau_l}{1 + i\omega\tau_l} \tag{A.5}$$

In order to process E(t) to estimate $E^*(\omega)$, the following steps should be taken:

1. Take an approximate derivative of $E(t)$ using Matlab's '`diff`' function to obtain $\dot{E}_1(t) = \dot{E}(t) - \sum_{l=1}^{L} E_l \delta(t)$
2. Take the '`fft`' of $\dot{E}_1(t)$ to obtain $E_1^*(\omega) = E^*(\omega) - E(0)$.
3. Obtain the complex modulus by taking $E^*(\omega) = E_1^*(\omega) + E(0)$.

A.1.3 Creep: Approach 2

The procedure used for processing creep data using approach 2 is:

1. Estimate and remove the linear term from $\varepsilon(t)$ to get $\varepsilon_1(t) = \varepsilon(t) - \beta(t)$.
2. Apply Nicolson's method of adding the correct ramp functions to the input stress $\sigma(t)$ and $\varepsilon_1(t)$

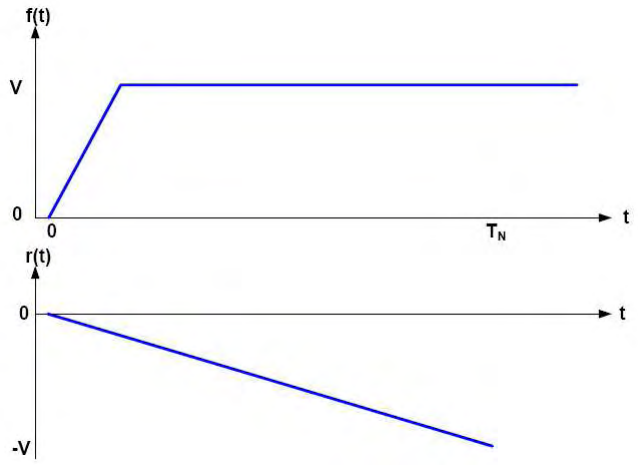

Figure A.1: Top figure: an aperiodic signal $f(t)$ in the form of a unit ramp with maximum amplitude V. Bottom figure: the ramp signal $r(t)$ added to original data according to Nicolson's method [24] to correct for errors associated with taking an FFT of data with the form of $f(t)$.

3. Take the FFT of signals created in step 2 to get $\tilde{\sigma}(\omega)$ and $\tilde{\varepsilon}_1(\omega)$.

4. Add the frequency response of the linear term to $\tilde{\varepsilon}_1(\omega)$ to get $\tilde{\varepsilon}(\omega)$

5. Take the ratio of the frequency responses to obtain $D^*(\omega) = \frac{\tilde{\varepsilon}(\omega)}{\tilde{\sigma}(\omega)}$ or $E^*(\omega) = \frac{\tilde{\sigma}(\omega)}{\tilde{\varepsilon}(\omega)}$.

A.2 Nicolson's Method

Nicolson's method [24] provides a way to correct for errors associated with taking an FFT of a unit ramp signal such as that depicted in the top sketch of figure A.1.

According to Nicolson, if the signal of interest $f(t)$, such as that depicted in figure A.1, is such that it remains a constant V after some time T_N, but 0 for $t < 0$, and we only have data up to T_N, then the Fourier transform of such a signal is given by,

$$F_T(\omega) = \int_0^{T_N} f(t)\exp(-i\omega t)dt \tag{A.6}$$

$$= \int_{-\infty}^{\infty} f(t)\exp(-i\omega t)dt - V\int_{T_N}^{\infty} \exp(-i\omega t)dt \tag{A.7}$$

$$= F(\omega) - \xi(\omega) \tag{A.8}$$

where $F_T(\omega)$ is the Fourier transform of the time domain data $f(t)$ over the interval $t = 0 \rightarrow t = T_N$, where T_N is assumed to be one period, after which $f(t)$ remains constant. By taking the Fourier transform of this section of $f(t)$, the result consists of the true Fourier transform of the signal $F(\omega)$

but has some error associated with it $\xi(\omega)$. To compensate for the loss of $\xi(\omega)$, a ramp function $r(t)$ of negative slope can be added to $f(t)$ prior to the Fourier transform. This ramp function is given in equation A.9 (the corresponding schematic is shown in figure A.1).

$$r(t) = -\frac{V}{T_N}t \tag{A.9}$$

To illustrate the effectiveness of Nicolson's method, a simple model $r_{t_0}(t)$ is generated of a function similar to the stimulus in stress relaxation and creep experiments. For simplicity purposes, the time of the ramp to the amplitude $V = 1$ is $t_0 = 1$ s as seen in figure A.2a. The corresponding ramp function $r(t)$ can be seen in figure A.2b. The summation of $r_{t_0}(t)$ and $r(t)$ can be seen in figure A.2c. The real and imaginary parts of the analytic Fourier transform ($r_{t_0}(\omega)$) of $r_{t_0}(t)$ can be seen in figures A.2d and e respectively. The analytic solution is given in equation A.10.

$$r_{t_0}(\omega) = \frac{\exp(-i\omega t_0) - 1}{\omega^2 t_0} \tag{A.10}$$

To illustrate the error associated with just taking the FFT of $r_{t_0}(t)$ directly, the Matlab function '`fft`' is used; the corresponding real and imaginary spectra are displayed in figure A.2f and g respectively. By using Nicolson's method and adding the ramp function before taking the FFT, it is seen in figures A.2h, and i that the correct real and imaginary spectra are obtained.

Nicolson's method is not the only way to successfully obtain a Fourier transform of such signal types. A more traditional method may have been to first take the derivative of the time domain data, take its Fourier transform, and then effectively integrate by dividing the result by $i\omega$ in the frequency domain to obtain a spectrum of the original signal. However, we do not use this technique because taking a derivative will amplify noise in the signal as well as suppress data with longer time constants associated with creep curves. Thus the method of choice for finding the Fourier transform of such signals is Nicolson's method.

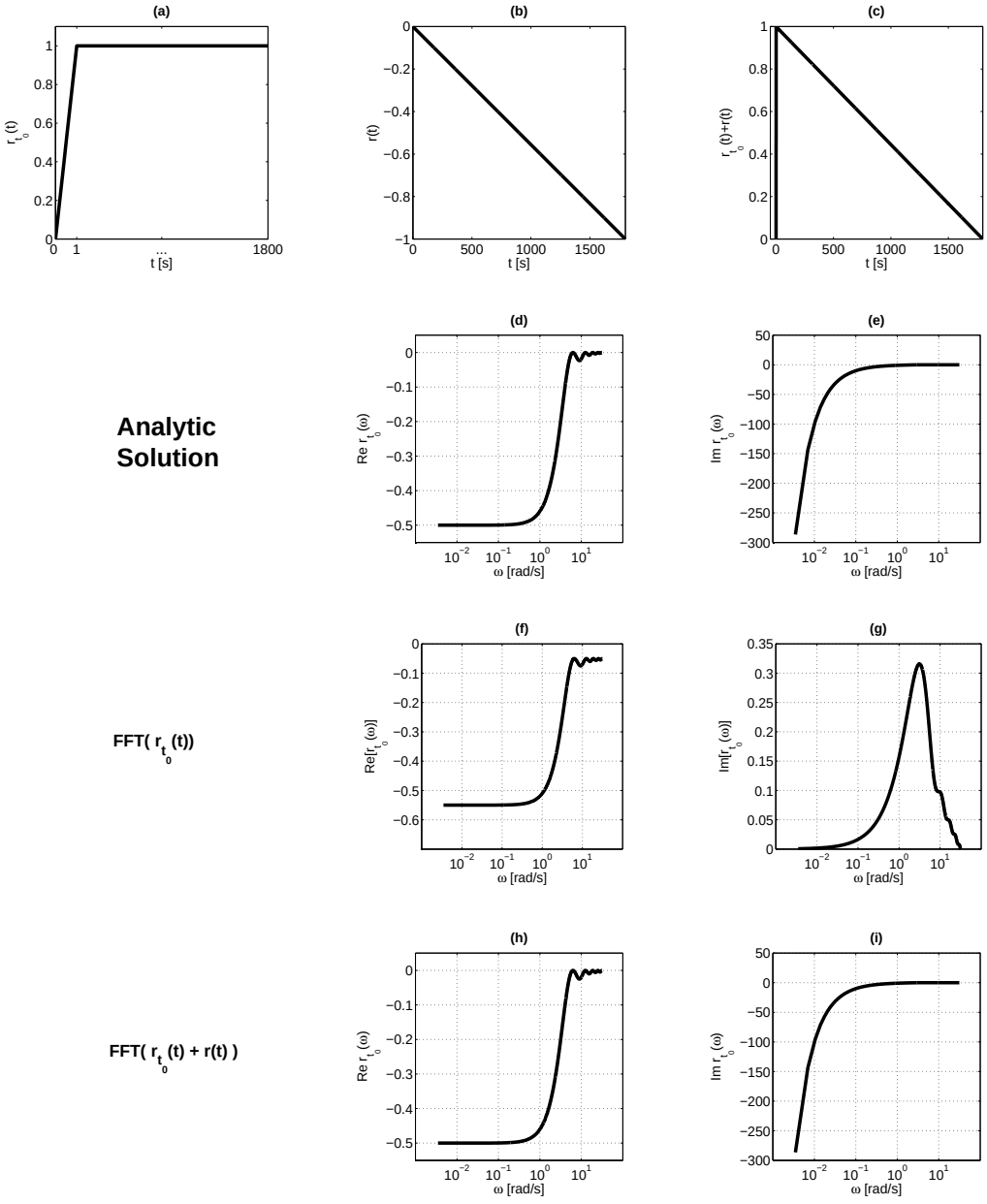

Figure A.2: Example of Nicolson's method for correcting error associated with taking the FFT of data in the form of a unit ramp.

References

[1] A. Bhattacharjee and M. Bansal. Collagen structure: The madras triple helix and the current scenario. *IUBMB Life*, 57:161–172, 2005.

[2] W. H. Brown. *Introduction to Organic Chemistry, Second Edition*. John Wiley and Sons, Inc., New Jersey, 2002.

[3] M. J. Buehler and S. Y. Wong. Entropic elasticity controls nanomechanics of single tropocollagen molecules. *Biophysical Journal*, 93:37–43, 2007.

[4] P. Chaturvedi, M. Insana, and T. Hall. Testing the limitations of 2-D companding for strain imaging using phantoms. *IEEE Transactions on Ultrasonics, Ferrorelectrics, and Frequency Control*, 45:1022–1031, 1998.

[5] C. Coussot, S. Kalyanam, R. Yapp, and M. F. Insana. Fractional derivative models for ultrasonic characterization of polymer and breast tissue viscoelasticity. *IEEE Transactions on Ultrasonics, Ferrorelectrics, and Frequency Control*, in press.

[6] C. W. N. Cumper and A. E. Alexander. The viscosity and rigidity of gelatin in concentrated aqueous systems II. rigidity. *Australian Journal of Scientific Research. Series A: Physical Sciences*, 5:153–159, 1952.

[7] M. Djabourov. Architecture of gelatin gels. *Contemporary Physics*, 29:273–297, 1988.

[8] B. Elenbaas and R. A. Weinberg. Heterotypic signaling between epithelial tumor cells and fibroblasts in carcinoma formation. *Experimental Cell Research*, 264:169–184, 2001.

[9] J. E. Fata, Z. Werb, and M. J. Bissell. Regulation of mammary gland branching morphogenesis by the extracellular matrix and its remodeling enzymes. *Breast Cancer Research*, 6:1–11, 2004.

[10] J. D. Ferry. *Viscoelastic Properties of Polymers, 3rd ed.* John Wiley and Sons, New York, 1980.

[11] J. R. Fried. *Polymer Science and Technology: 2nd Edition*. Prentice Hall Professional Technical Reference, New Jersey, 2003.

[12] J. R. Fried. *Polymer Science and Technology: Second Edition*. Pearson Education, Inc., New Jersey, 2003.

[13] B. S. Garra, E. I. Cespedes, J. Ophir, S. R. Spratt, R. A. Zuurbier, C. M. Magnant, and M. F. Pennanen. Elastography of breast lesions: Initial clinical results. *Radiology*, 202:79–86, 1997.

[14] L. E. Gerweck, S. Vijayappa, and S. Kozin. Tumor pH controls the in vivo efficacy of weak acid and base chemotherapeutics. *Molecular Cancer Therapeutics*, 5:1275–1279, 2006.

[15] R. J. Gillies, N. Raghunand, M. L. Garcia-Martin, and R. A. Gatenby. pH imaging. *IEEE Engineering in Medicine and Biology Magazine*, 23:57–64, 2004.

[16] F. Gobeaux, G. Mosser, A. Anglo, P. Panine, P. Davidson, M. M. Giraud-Guille, and E. Belamie. Fibrillogenesis in dense collagen solutions: A physiochemical study. *Journal of Molecular Biology*, 376:1509–1522, 2008.

[17] T. J. Hall, M. Bilgen, M. F. Insana, and T. A. Krouskop. Phantom materials for elastography. *IEEE Transactions on Ultrasonics, Ferrorelectrics, and Frequency Control*, 44:1355–1365, 1997.

[18] J. H. Highberger. The isoelectric point of collagen. *Journal of the American Chemical Society*, 61:2302–2303, 1939.

[19] D. I. Hitchcock. The isoelectric point of a standard gelatin preparation. *The Journal of General Physiology*, 14:685–699, 1931.

[20] C. Joly-Duhamel, D. Hellio, A. Ajdari, and M. Djabourov. All gelatin networks: 2. the master curve for elasticity. *Langmuir*, 18:7158–7166, 2002.

[21] S. Kalyanam, R. D. Yapp, and M. F. Insana. Poroviscoelastic behavior of gelatin hydrogels under compression: Implications for bioelasticity imaging. *ASME Journal of Biomechanical Engineering*, in review.

[22] J. Liu, C. K. Abbey, and M. F. Insana. Linear approach to axial resolution in elasticity imaging. *IEEE Transactions on Ultrasonics, Ferrorelectrics, and Frequency Control*, 51:716–725, 2004.

[23] B. Mohanty, A. Gupta, H. B. Bohidar, and S. Bandyopadhyay. Effect of gelatin molecular charge heterogeneity on formation of intermolecular complexes and coacervation transition. *Journal of Polymer Science: Part B: Polymer Physics*, 45:1511–1520, 2007.

[24] A. M. Nicolson. Forming the fast Fourier transform of a step response in time-domain metrology. *Electronics Letters*, 9:317–318, 1973.

[25] A. V. Oppenheim, A. S. Willsky, and S. Hamid Nawab. *Signals and Systems: Second Edition*. Prentice Hall, New Jersey, 1997.

[26] C. Pellot-Barakat, M. Sridhar, K. K. Lindfors, and M. F. Insana. Ultrasonic elasticity imaging as a tool for breast cancer diagnosis and research. *Current Medical Imaging Reviews*, 2:157–164, 2006.

[27] H. Ponnekanti, J. Ophir, Y. Huang, and I. Cespedes. Fundamental mechanical limitations on the visualization of elasticity contrast in elastography. *Ultrasound in Medicine and Biology*, 21:533–543, 1995.

[28] Y. Qiu, M. Sridhar, J. K. Tsou, K. K. Lindfors, and M. F. Insana. Ultrasonic viscoelasticity imaging of nonpalpable breast tumors: preliminary results. *Academic Radiology*, in press.

[29] B. A. Roeder, K. Kokini, J. E. Sturgis, J. P. Robinson, and S. L. Voytik-Harbin. Tensile mechanical properties of three-dimensional type I collagen extracellular matrices with varied microstructure. *ASME Journal of Biomechanical Engineering*, 124:214–222, 2002.

[30] G. P. Seehra and F. H. Silver. Viscoelastic properties of acid- and alkaline-treated human dermis: a correlation between total surface charge and elastic modulus. *Skin Research and Technology*, 12:190–198, 2006.

[31] A. C. Sharma, M. S. Soo, G. E. Trahey, and K. R. Nightingale. Acoustic radiation force impulse imaging of in vivo breast masses. *IEEE Ultrasonics Symposium*, pages 728–731, 2004.

[32] R. Sinkus, M. Tanter, T. Xydeas, S. Catheline, J. Bercoff, and M. Fink. Viscoelastic shear properties of in vivo breast lesions measured by MR elastography. *Magnetic Resonance Imaging*, 23:159–165, 2005.

[33] M. Sridhar and M. F. Insana. Ultrasonic measurements of breast viscoelasticity. *Medical Physics*, 34:4757–4767, 2007.

[34] M. Sridhar, J. Liu, and M. F. Insana. Elasticity imaging of polymeric media. *ASME Journal of Biomechanical Engineering*, 129:259–272, 2007.

[35] M. Sridhar, J. Liu, and M. F. Insana. Viscoelasticity imaging using ultrasound: Parameters and error analysis. *Physics in Medicine and Biology*, 52:2425–2443, 2007.

[36] M. Stoeckelhuber, P. Stumpf, E. A. Hoefter, and U. Welsch. Proteoglycan-collagen associations in the non-lactating human breast connective tissue during the menstrual cycle. *Histochemistry and Cell Biology*, 118:221–230, 2002.

[37] N. W. Tschoegl. *The Phenomenological Theory of Linear Viscoelastic Behavior*. Springer, New York, 1989.

[38] R. Usha and T. Ramasami. Effect of pH on dimensional stability of rat tail tendon collagen fiber. *Journal of Applied Polymer Science*, 75:1577–1584, 2000.

[39] A. Veis. *The Macromolecular Chemistry of Gelatin*. Academic Press, New York, 1964.

[40] R. D. Yapp and M. F. Insana. pH induced contrast in viscoelasticity imaging of biopolymers. *Physics in Medicine and Biology*, in review.

[41] R.D. Yapp, S. Kalyanam, and M.F. Insana. Molecular and structural analysis of viscoelastic properties. *Proceedings of SPIE Medical Imaging*, 6511:65111Y–1 – 65111Y–11, 2007.

[42] G. Zhang. Evaluating the viscoelastic properties of biological tissues in a new way. *J Musculoskelet Neuronal Interact*, 5:85–90, 2005.